

Data Fusion of AIRS and CrIMSS Near Surface Air Temperature

P. Kalmus¹, H. Nguyen¹, J. Roman¹, T. Wang¹, Q. Yue¹, Y. Wen², J. Hobbs¹,
and A. Braverman¹

¹Jet Propulsion Laboratory, California Institute of Technology, Pasadena, CA, 91109

²Department of Geography, University of Florida, Gainesville, FL, 32611

Key Points:

- We demonstrate spatial statistical fusion for Level 2 remote sensing datasets which estimate the same observable
- We introduce a new daily and nightly fused near-surface air temperature product from satellite hyperspectral sounders over CONUS
- The fused product decreases bias and RMSE by 1 K and 25% respectively relative to input datasets, averaged over the domain of the study

Corresponding author: Peter Kalmus, peter.m.kalmus@jpl.nasa.gov

Abstract

We present a near surface air temperature (NSAT) fused data product over the contiguous United States using Level 2 data from the Atmospheric Infrared Sounder (AIRS), on the Aqua satellite, and the Cross-track Infrared Microwave Sounding Suite (CrIMSS), on the Suomi National Polar-orbiting Partnership (SNPP) satellite. We create the fused product using Spatial Statistical Data Fusion (SSDF), a procedure for fusing multiple datasets by modeling spatial dependence in the data, along with ground station data from NOAA’s Integrated Surface Database (ISD) which is used to estimate bias and variance in the input satellite datasets. Our fused NSAT product is produced twice daily and on a 0.25-degree latitude-longitude grid. We provide detailed validation using withheld ISD data and comparison with ERA5-Land reanalysis. The fused gridded product has no missing data; has improved accuracy and precision relative to the input satellite datasets, and comparable accuracy and precision to ERA5-Land; and includes improved uncertainty estimates. Over the domain of our study, the fused product decreases daytime bias magnitude by 1.7 K and 0.5 K, nighttime bias magnitude by 1.5 K and 0.2 K, and overall RMSE by 35% and 15% relative to the AIRS and CrIMSS input datasets, respectively. Our method is computationally fast and generalizable, capable of data fusion from multiple datasets estimating the same quantity. Finally, because our product reduces bias, it produces long-term datasets across multi-instrument remote sensing records with improved bias stationarity, even as individual missions and their data records begin and end.

Plain Language Summary

We have used a data fusion technique called spatial statistical data fusion (SSDF) to create an improved near surface air temperature (NSAT) dataset by fusing two separate satellite datasets. NSAT is important for a variety of applications, such as drought, wildfire, and extreme heat research and prediction. The two input NSAT datasets come from the AIRS instrument on the Aqua satellite, and the CrIMSS suite on the SNPP satellite. Our fused NSAT product is produced twice daily and on a 0.25-degree latitude-longitude grid. We also performed a detailed validation using withheld reference data (which was not included in the bias-correction data) and comparison with ERA5-Land reanalysis. The new SSDF product has no missing data; has improved accuracy and precision relative to the input satellite datasets, and comparable accuracy and precision to ERA5-Land; and includes improved uncertainty estimates. SSDF is computationally fast and generalizable, capable of data fusion from multiple datasets so long as they estimate the same quantity. Finally, because our product reduces bias, it provides a means of creating high-quality continuous long-term datasets across the years, as individual satellite missions and their data records begin and end.

1 Introduction

Data fusion is the combining of multiple datasets into a single dataset with improved properties relative to the input datasets (for a recent review, see Ghamisi et al. (2019)). Near-surface air temperature (NSAT, the air temperature at a height of 2 m above the surface) is a fundamental variable that critically affects life on the Earth’s surface, and an Essential Climate Variable. Here, we describe the use of spatial statistical data fusion (SSDF) to fuse two Level 2 (L2) satellite NSAT datasets into a single product at 0.25-degree spatial resolution on a twice-daily basis (one daytime and one nighttime estimate per day) over the contiguous United States (CONUS) and adjacent parts of North America. SSDF utilizes spatial dependence within and between the datasets to improve estimates at any given point, including at locations not covered by the input data.

64 As the Earth continues to rapidly heat due to human emissions of greenhouse
65 gases, NSAT remote sensing records are becoming increasingly important for a number
66 of critical science and applied science areas such as health, urban planning, hydrology
67 and water, ecology and conservation, and wildfire prediction. NSAT data records
68 have been produced by a variety of methods which are suited for different purposes.
69 One method is to collect NSAT measurements from ground stations; one example
70 of this type of dataset is the Integrated Surface Database, or ISD (A. Smith et al.,
71 2011). Ground station measurements are relatively accurate, but they are sparse
72 point-source measurements with some regions of the planet having less coverage than
73 others. These strengths and weaknesses make them suitable for use as reference data
74 for validation purposes. Another type of NSAT dataset can be created by filtering and
75 processing these raw NSAT ground measurements into space-filled, gridded climate
76 records useful for climate analysis and climate model validation. These climate records
77 are typically monthly mean products at low resolution, such as the 1-degree resolution
78 Berkeley Earth Monthly Land+Ocean dataset (Rohde & Hausfather, 2020). Berkeley
79 Earth is also experimenting with daily and 0.25-degree-resolution datasets. A third
80 strategy for estimating NSAT is reanalysis, which uses multiple data sources (including
81 satellite data) and dynamical weather models to create dynamically consistent gridded
82 fields. As computational power and algorithm efficiencies have increased, so have the
83 spatial resolutions of reanalysis datasets. An example is the European Centre for
84 Medium-Range Weather Forecasts (ECMWF) Reanalysis 5 (ERA5)-Land reanalysis
85 NSAT dataset (Hennermann & Berrisford, 2019), which has hourly temporal resolution
86 and a spatial resolution of 0.1 degrees, the highest available at the time of writing.
87 Finally, NSAT can be estimated from satellite remote sensing. NSAT can be retrieved
88 from imaging instruments which can estimate land surface temperature (LST) at high
89 resolutions, although obtaining NSAT from LST requires regression modeling which
90 introduces its own errors. An example of NSAT modeled from LST is the EUSTACE
91 project (Good, 2015; Rayner et al., 2020), which produced global daily NSAT at 0.25-
92 degree resolution. NSAT can also be estimated from atmospheric temperature profiles
93 from infrared sounders using interpolation to the surface pressure level, such as the
94 AIRS and CrIMSS products used in this study and described below in Section 2.1.

95 Our data-fusion methodology, SSDF, exists within a geostatistical framework
96 which is a part of the broader area of spatial statistics. Specifically, SSDF is de-
97 signed to provide the principled error characterization and error propagation within
98 data fusion for massive remote sensing data (Nguyen et al., 2012). SSDF has been
99 demonstrated previously in the context of data fusion of L2 satellite remote sensing
100 datasets. L2 datasets are geophysical quantities inferred or “retrieved” from the pri-
101 mary observations of radiances by the orbiting instruments (known as “Level 1” data).
102 The SSDF methodology we utilize here was first used to fuse L2 aerosol optical depth
103 from the Multi-angle Imaging Spectroradiometer (MISR) and the Moderate Resolution
104 Imaging Spectroradiometer (MODIS) aboard the Terra platform. It was subsequently
105 demonstrated in the fusion of L2 total column CO₂ concentration (XCO₂) from the
106 Atmospheric Infrared Sounder (AIRS) aboard the Aqua platform and XCO₂ from the
107 Orbiting Carbon Observatory-2 (OCO-2) (Nguyen et al., 2014). In addition, an SSDF
108 variant called local kriging was used to produce fused estimates of XCO₂ from GOSAT
109 (Hammerling et al., 2012). In the current work, we describe the creation of the first
110 long data record produced by SSDF, and the first data fusion of NSAT by any method.

111 L2 datasets can present certain challenges and limitations to end users which
112 can be mitigated through data fusion. Instantaneous snapshots are obtained at a
113 large number of spatial and temporal fields of regard determined by orbital and sensor
114 geometry, and therefore do not fall on a regular grid. Data coverage is spatially
115 and temporally incomplete due to clouds, gores (spaces between orbit tracks), and
116 faults due to “single-event upsets” often attributed to cosmic rays. L2 data can have

117 large errors relative for example to reanalysis datasets, and uncertainty estimates, if
118 reported, may not accurately represent the true error.

119 Our SSDF NSAT product combines two input remote sensing datasets: L2 NSAT
120 from AIRS, and L2 NSAT from the Cross-track Infrared Microwave Sounding Suite
121 (CrIMSS) on the Suomi National Polar-orbiting Partnership (SNPP) platform. These
122 L2 datasets are created using two independent retrieval algorithms with different first-
123 guess strategies. We also use information content from in situ ground station networks
124 from NOAA’s Integrated Surface Database (ISD) to determine uncertainties in the two
125 remote sensing datasets which are needed to perform fusion, and to validate the SSDF
126 product and its associated uncertainty estimates. We randomly divide the ISD data
127 into training and testing sets to perform these two separate functions.

128 Our fused SSDF NSAT product has the following key advantages over either of
129 the input remote sensing datasets:

- 130 1. SSDF fills spatial gaps;
- 131 2. SSDF produces estimates on a regular 0.25-degree spatial grid;
- 132 3. SSDF reduces bias and variance relative to a reference in situ dataset;
- 133 4. SSDF produces improved uncertainty estimates;
- 134 5. SSDF improves long-term stationarity relative to the input datasets.

135 The rest of the paper is organized as follows. We first describe the input datasets
136 and methodology. Then we present the SSDF NSAT product, and the results of val-
137 idation against withheld ISD surface station data. We also compare the SSDF fused
138 NSAT product to the individual input remote sensing datasets, and to ERA5-Land
139 reanalysis. In the process of validating our SSDF product, we also produce the most
140 thorough validation study to date of the AIRS V7 and SNPP-CrIMSS-CLIMCAPS
141 V2 NSAT products over CONUS. We conclude with a discussion of advantages, limi-
142 tations, and potential future work.

143 2 Data and methods

144 Performing and evaluating SSDF involves five major steps: (1) Obtaining and
145 filtering input remote sensing datasets that estimate the same quantity; (2) Match-
146 ing the remote sensing datasets to a reference in situ dataset in space and time; (3)
147 Using these matched data pairs (“matchups”) to characterize the input datasets via
148 estimation of their bias and variance relative to the reference estimate; (4) Performing
149 the SSDF calculations; and (5) Validating the results using withheld data from the
150 reference dataset. The method and the specific datasets used in our NSAT dataset are
151 described in the following subsections.

152 2.1 Satellite NSAT data

153 The input satellite datasets come from two hyperspectral infrared sounders and
154 retrieval algorithms. The Aqua platform that carries AIRS launched in 2002 in a
155 sun-synchronous polar orbit, with equator crossing times of approximately 1:30 P.M.
156 and 1:30 A.M. for ascending (south to north) and descending (north to south) nodes,
157 respectively. AIRS is an infrared grating spectrometer with 2378 channels, spanning
158 3.7 to 15.4 μm (Chahine et al., 2006). Power to critical channels of the Aqua satellite’s
159 Advanced Microwave Sounding Unit (AMSU)-A2 was lost in September 2016 (Yue et
160 al., 2017). AMSU-A2 complemented the AIRS instrument in atmospheric temperature
161 and moisture profile retrievals, and was especially informative for moisture profiles.
162 The Cross-track Infrared Sounder (CrIS) and the Advanced Technology Microwave
163 Sounder (ATMS) instruments launched onboard the SNPP platform in 2012. SNPP

164 is in the same orbital plane as Aqua, but at a higher altitude (824 km as opposed
 165 to 705 km), with equator crossing times also approximately 1:30 P.M. and 1:30 A.M.
 166 Together, these two instruments are known as SNPP-CrIMSS (Cross-track Infrared
 167 Microwave Sounder Suite). SNPP-CrIS experienced an anomaly on May 21, 2021
 168 which resulted in the loss of the longwave infrared channels. Another instance of
 169 CrIMSS is flying on the JPSS-1 (Joint Polar Satellite System, also known as J1 or
 170 NOAA-20) which launched on November 2017. Data from J1-CrIMSS is not used in
 171 this study, but could be used in future SSDF products.

172 For obtaining Aqua-AIRS temperature soundings, we use the AIRS-team Version
 173 7 L2 “infrared-only” temperature retrieval algorithm (Susskind et al., 2014), a least
 174 squares estimate using singular value decomposition regularization and cloud-cleared
 175 radiances. Stochastic Cloud Clearing Neural Network (SCCNN) which is trained to
 176 ECMWF fields (Blackwell, 2005) as a first guess, then refines to a final estimate. We
 177 choose the “infrared-only” retrieval for our study due to the 2016 loss of AMSU-A2,
 178 but we note that this retrieval uses information from the satellite’s other microwave
 179 sounder, AMSU-A1 (Yue et al., 2020). The retrieval uncertainty is estimated via a
 180 regression model using eleven retrieval diagnostic quantities as predictors; the regres-
 181 sion coefficients are trained on two days of retrievals (9/29/04 and 2/24/07) using
 182 ECMWF 3-hour forecasts as a reference dataset (Susskind et al., 2014; Thrastarson
 183 et al., 2020). Each individual retrieval has a nominal horizontal resolution of 45 km
 184 comprised of nine 15 km fields of view in a 3x3 matrix, and each swath contains 30
 185 retrievals across its width and 45 along track. The product is organized nominally in
 186 240 “orbital granules” per day (AIRS Project, 2020).

187 For obtaining SNPP-CrIMSS temperature soundings, we use the Community
 188 Long-term Infrared Microwave Coupled Atmospheric Product System (CLIMCAPS)
 189 Version 2 L2 temperature retrieval, which uses a hybrid optimal estimation methodol-
 190 ogy with a first guess from the Modern-Era Retrospective Analysis for Research and
 191 Applications version 2 (MERRA2) (N. Smith & Barnet, 2020), and information from
 192 both the CrIS and ATMS instruments. Like the AIRS-team retrieval, CLIMCAPS
 193 uses nine approximately 15 km fields of view in a 3x3 field of regard of 45 km, and
 194 performs cloud clearing using L1 radiances. CLIMCAPS uncertainty is estimated and
 195 propagated sequentially via error covariance matrices in stages (N. Smith & Barnet,
 196 2019). CLIMCAPS produces a combined infrared and microwave retrieval at two
 197 spectral resolutions: Nominal Spectral Resolution (NSR) and Full Spectral Resolution
 198 (FSR). We use the CLIMCAPS-SNPP NSR product to create our SSDF product, since
 199 it begins in 2012 whereas the FSR record only begins on November 2, 2015. In what
 200 follows, we refer to this product as “CrIMSS-CLIMCAPS” or sometimes as “CrIMSS.”
 201 An overview of the AIRS-team and CLIMCAPS retrievals is available online (AIRS
 202 team, n.d.), and a detailed comparison of the two retrievals applied to AIRS L1 data
 203 is available, including relative strengths and weaknesses can be found in (Yue et al.,
 204 2021).

205 NSAT is obtained from the vertically-resolved temperature profiles (with 100
 206 pressure levels) via interpolation to the surface pressure for each field of regard (Olsen
 207 et al., 2017). The profile temperatures immediately above and below the surface
 208 are used for the interpolation, unless the level above is within 5 hPa of the surface
 209 pressure. In that case, the two levels above the surface are used. We include only L2
 210 NSAT retrievals from AIRS V7 IR-only and CrIMSS-CLIMCAPS products with data
 211 quality flags ‘good’ or ‘best.’

212 **2.2 In situ NSAT data**

213 The National Oceanic and Atmosphere Administration (NOAA) Integrated Sur-
 214 face Database (ISD) is a global database of near-surface meteorological observations

215 compiled from over a hundred systems of ground stations (A. Smith et al., 2011). The
 216 record extends back to the 1950s, although new stations have been added on a con-
 217 tinual basis as available, improving coverage over time. Today ISD consists of more
 218 than 35,000 surface weather stations globally, 14,000 of which remain active. Figure 1
 219 shows the spatial coverage of ISD stations in North America.

220 We use sub-hourly NSAT measurements gathered from over 7000 stations in
 221 North America as our reference dataset, for bias and variance estimation and for valida-
 222 tion. No data are perfect, but the ISD errors are small relative to the errors in the input
 223 remote sensing datasets (see Figure 7). Naturally ventilated screened surface station
 224 air temperature measurements are accurate to ± 0.1 K in most circumstances (Harrison
 225 & Burt, 2021). ISD data come with a set of ten data quality flags, indicating various
 226 problems and levels of quality. We only use ISD data flagged as highest quality, i.e.,
 227 data must be flagged with either 1 (‘Passed all quality control checks’) or 5 (‘Passed
 228 all quality control checks, data originate from an NCEI data source’).

229 We chose ISD ground stations as our reference dataset for the following reasons:
 230 (1) it is not reanalysis, which assimilates AIRS and SNPP-CrIMSS information, as
 231 well as information from dynamical weather modeling; (2) ISD is among the most
 232 comprehensive ground station datasets available; (3) ISD NSAT estimates have low
 233 errors relative to remote sensing estimates.

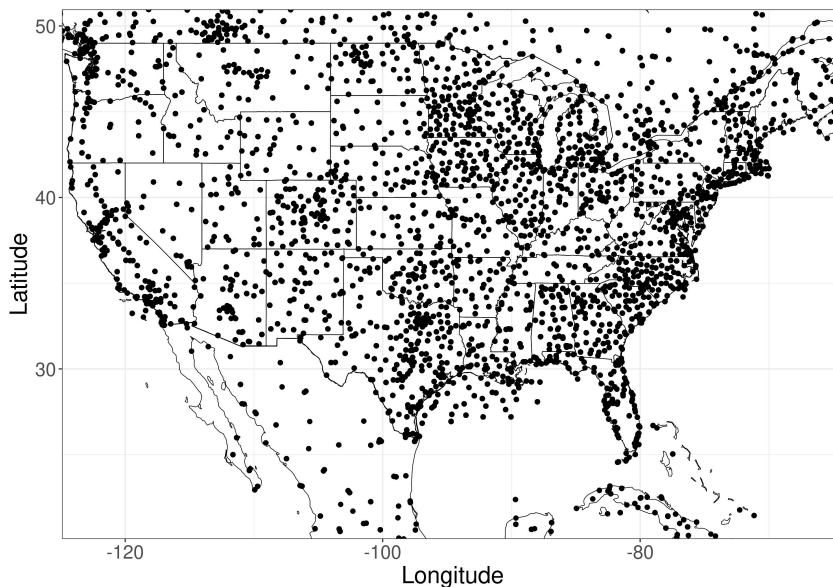


Figure 1: Spatial coverage of the ISD stations over North America. Note that ISD is a global dataset.

234 **2.3 Reanalysis NSAT data**

235 We also compare the SSDF NSAT results to ECMWF Reanalysis 5 (ERA5)-
 236 Land reanalysis data. The ERA5 is the fifth-generation global atmospheric reanalysis
 237 from ECMWF, replacing the ERA-Interim reanalysis which stopped being produced
 238 on August 31, 2019. Newly reprocessed datasets along with recent instruments have
 239 been assimilated into the ERA5 that could not be ingested into the ERA-Interim
 240 (Hennermann & Berrisford, 2019). We note that some AIRS spectral channels under

241 clear conditions are incorporated into ECMWF reanalysis (McNally et al., 2006), but
 242 that ISD data are not.

243 We use hourly ERA5-Land output which is a high-resolution version of the land
 244 component of the ERA5 reanalysis. ERA5-Land 2 m air temperature was chosen over
 245 the full ERA5 reanalysis for its finer spatial resolution of 0.1x0.1 degrees and hourly
 246 temporal resolution.

247 **2.4 Bias and variance estimation**

248 Biases and variances of input data sources are the key to high-quality data fusion.
 249 SSDF assumes input data are unbiased, and weights them by the inverse of their
 250 respective variances. This minimizes output errors of the fused estimates. Therefore,
 251 data must be bias-corrected before SSDF ingestion, and the quality of the final fused
 252 product depends on the quality of uncertainty estimates for the inputs.

253 To estimate bias and variance for satellite footprints, we create an ensemble
 254 of “matchups”: matched pairs of satellite and ISD station estimates that are close
 255 in space (less than 100 km apart) and time (less than an hour apart). For a given
 256 period, the matchups are sorted into 240 km (\sim two-degree) diameter hexagonal spatial
 257 bins based on satellite footprint location, with three-day time bins (day of interest,
 258 along with preceding and following days). We empirically tested different time bins
 259 (monthly, seven days, and three days) for aggregating matchups for determining bias
 260 and variance, and the three-day time bins minimized the mean standard deviation of
 261 a sample SSDF product over CONUS, while allowing for adequate sample size. This
 262 binning is the basis for quantifying bias and variance for all satellite footprints in a
 263 given space-time cell. We randomly select 1% of the ISD matchup pairs to withhold for
 264 validation (we do not withhold entire ISD stations). We chose a relatively small amount
 265 to withhold in order to maximize the information content for the SSDF product.

266 To obtain the matchups we apply the following steps.

- 267 1. Given an ISD observation at location \mathbf{s} and time $t^I(\mathbf{s})$, select the AIRS granule
 268 (1 of 240) with the closest time to $t^I(\mathbf{s})$.
- 269 2. Within this granule, select all L2 retrievals within 100 km of \mathbf{s} and 1 hour of
 270 $t^I(\mathbf{s})$.
- 271 3. If Step 2 results in more than 1 retrieval, select the one closest in spatial distance.

272 Note that these steps will result in a one-to-one match between an ISD obser-
 273 vation and a single AIRS footprint. Some ISD observations may have no correspond-
 274 ing AIRS match, in which case no matchup is returned. We next tessellate a fixed
 275 hexagonal spatial grid over CONUS and find the biases and variances using matchups
 276 aggregated over 3 days within each grid cell, as follows:

- 277 I. To compute a bias on day d and mode j (day or night) and in hexagonal grid
 278 cell i , we find the set of all valid (i.e., non-null) AIRS-ISD matchups from Steps
 279 1 to 3 above such that,
 - 280 (a) the AIRS data come from mode j ,
 - 281 (b) the AIRS footprint belongs within the grid cell i ,
 - 282 (c) the ISD date is in $(d - 1, d, d + 1)$.
- 283 II. The bias and variance for day d , mode j , and grid cell i are then computed
 284 using the set of paired ISD-AIRS matchups.

285 Bias and variance estimation for CrIMSS follows the same procedure. For bias
 286 correction, given an instrument observation at location \mathbf{s} on day d and mode j , we

287 compute the corresponding bias within the grid cell which contains \mathbf{s} for day d and
 288 mode j , and we subtract it from the instrument’s NSAT value. For more detail on the
 289 bias and variance estimation process, please refer to Appendix A.

290 After the bias field is estimated for a given dataset relative to the ISD reference
 291 dataset, every datum in that dataset is then bias-corrected. After the variance field
 292 is estimated for a given dataset, every datum in that dataset is assigned a variance
 293 estimate which is then used in the SSDF algorithm to weight the datum.

294 2.5 Data fusion methodology

295 SSDF is an algorithm for fusing multiple remote sensing datasets by leveraging
 296 spatial dependence in the data, also known as kriging or optimal interpolation (Cressie,
 297 1993). Remote sensing data from different instruments in general are heterogeneous.
 298 By this we mean that the input remote sensing data sets may have different spatial
 299 footprints, sampling patterns, and measurement error characteristics. SSDF accounts
 300 for these heterogeneities by using a spatial statistical model that expresses the rela-
 301 tionships between the true quantity of interest at a particular location, and all the
 302 observations at all locations from all data sources.

303 We note that the main requirement of SSDF is that the different instruments in
 304 question (e.g., AIRS and CrIMMS) must be observing the same geophysical quantity
 305 of interest (e.g., NSAT). We assume that after bias correction, the retrievals from
 306 both instruments are unbiased relative to the true underlying process. We also assume
 307 that we have standard deviation estimates that characterize the relative informational
 308 content between the instruments.

309 One of the challenges encountered when applying spatial interpolation via tradi-
 310 tional kriging to remote sensing data is the massive data sizes involved. In traditional
 311 kriging, the computational complexity of the algorithm is $O(N^3)$ due to the need to
 312 invert an $N \times N$ covariance matrix \mathbf{C} , where N is the number of data points. This
 313 inversion makes traditional kriging infeasible for datasets with N on the order of tens
 314 of thousands of data points or larger. To account for this, we use a scalable vari-
 315 ant of kriging that employs a dimension-reduction technique (Spatial Random Effects
 316 modeling) to parameterize the matrix \mathbf{C} as a rank- r update to a diagonal matrix,
 317 where $r \ll N$. This allows us to invert the covariance matrix \mathbf{C} analytically us-
 318 ing the Sherman-Morrison-Woodbury formula with computational complexity $O(Nr^2)$
 319 (Cressie & Johannesson, 2008). SSDF is essentially an extension of Fixed-Ranked Krig-
 320 ing (FRK) for combining multiple datasets. Indeed, SSDF works by concatenating all
 321 the datasets into a meta-dataset (with each data point encoded with a value, location,
 322 and variance estimate) and then applying the FRK algorithm. Therefore, SSDF can
 323 easily generalize to more datasets than two, and it can also be applied to a single
 324 dataset (a sub-case needed for the AIRS-only part of the multi-instrument record,
 325 from 2002-2012), without mathematical modification.

326 A second challenge with traditional kriging is handling arbitrary spatial foot-
 327 prints of the input datasets and those of the output grid. Gotway and Young (2002)
 328 identified this “change of support” problem of inferring a spatial process at one res-
 329 olution from data at another resolution. However, their solution is computationally
 330 intensive, requiring integration over footprints and making it difficult to do parameter
 331 estimation for general non-linear covariance classes. In SSDF the SRE model is linear,
 332 which makes change of support and the associated parameter estimation straightfor-
 333 ward (Nguyen et al., 2012).

334 As a scalable variant of Gaussian process prediction (Cressie, 1993), SSDF pro-
 335 vides two other advantages over other non-statistical data fusion approaches such as
 336 binning or non-parametric methods such as machine learning. First, the standard

337 errors are optimized because SSDF minimizes errors relative to the unknown true pro-
 338 cess; SSDF estimates are therefore “best linear unbiased estimates.” Within the class
 339 of linear estimators, this method produces the smallest prediction errors. In addition,
 340 SSDF provides a statistically principled method for estimating uncertainties. Mini-
 341 mizing errors and quantifying uncertainties allows SSDF to create more accurate and
 342 usable data products from input datasets.

343 For the full mathematical formulation of SSDF, see Appendix B.

344 2.6 Dataset preparation for validation

345 We validate our SSDF product using a randomly chosen reserved 1% of the ISD
 346 dataset. We match up SSDF, AIRS, CrIMSS, and ERA5 estimates to withheld ISD
 347 data using a 100 km and 1 hour matchup criterion (see Section 2.4 for more detail).
 348 These matchup datasets generally differ in their coverage; for instance, an SSDF es-
 349 timate might be matched to an ISD observation at a location where there are no
 350 nearby AIRS or CrIMSS estimates. Therefore, to mitigate the effect of biases due to
 351 differing spatial and temporal coverage in these matchup pairs, we also require that
 352 SSDF estimates are also close to (within the same matchup distance and time) of at
 353 least one datum from the comparison dataset. This matchup procedure generates mul-
 354 tiple paired datasets: ISD-AIRS, ISD-CrIMSS, ISD-SSDF, and ISD-ERA5, allowing
 355 comparison, for example, of pairs of datasets such as AIRS and SSDF(AIRS) (i.e., a
 356 subset of the SSDF points matched up to AIRS points) which have the same number
 357 of samples, each of which is collocated in space and time within the matchup criterion.
 358 To put this another way, the reason we have separate plot traces for SSDF(AIRS) and
 359 SSDF(CrIMSS) is to allow an apples-to-apples comparison despite differing spatial
 360 coverage of the AIRS, CrIMSS, ERA5, and SSDF datasets.

361 The choices of a 1% test ISD dataset and this matchup scheme results in over
 362 4000 AIRS-SSDF sample pairs and over 13,000 CrIMSS-SSDF sample pairs for 2013,
 363 a typical year.

364 3 Results

365 3.1 SSDF product overview

366 We produced fused NSAT using two satellite input datasets over North America
 367 between 25 N and 50 N. We chose to fuse the AIRS and SNPP-CLIMCAPS products
 368 because the orbits of these satellites have similar overpass times of approximately
 369 1:30 and 13:30 local solar time, and the records extend back to at least 2013. We
 370 note that although we initially restrict our product to CONUS, the two input L2
 371 retrievals provide global coverage, and that we plan to extend our SSDF product to
 372 global land surfaces in the future. We produce two products, a main product from
 373 both AIRS and SNPP-CrIMSS which runs from November 28 2012 through 2020 and
 374 which we will denote SSDF-AC; and a long-record product with just AIRS, which
 375 runs from August 31 2002 through 2020 and which we will denote SSDF-A. These
 376 two product lines were created identically, with the only difference being that the list
 377 of input data tuples (bias-corrected NSAT, latitude, longitude, and variance) fed to
 378 the SSDF algorithm consisted of tuples from either two remote sensing datasets or
 379 just one. Between 2013 and 2020 there were 32 days and 30 nights with no AIRS
 380 data, and 29 days and 24 nights with no SNPP-CLIMCAPS data. Because outages
 381 happened not to occur for both input datasets on the same day or night over this
 382 period, the SSDF-AC product was created from only the single dataset when necessary,
 383 thus creating a continuous record. The SSDF-A record has 74 missing daily files
 384 due to AIRS outages, often due to single event upsets (for a list of AIRS outages,

385 see <https://airs.jpl.nasa.gov/data/outages/>). In what follows, if not otherwise
 386 specified, “SSDF” refers to SSDF-AC.

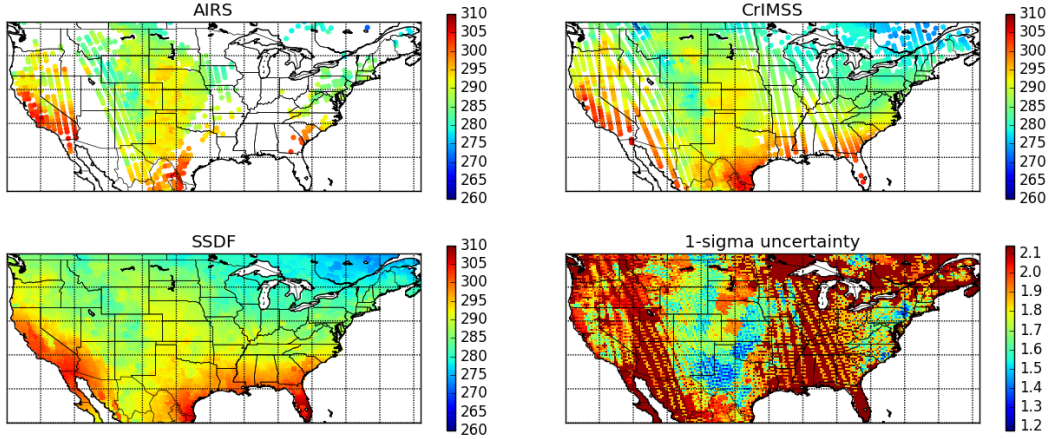


Figure 2: Sample data fusion satellite NSAT inputs, SSDF NSAT results, and uncertainty estimates for 2015 October 31, day. The top two plots show maps of the input satellite NSAT data ingested into the SSDF product (restricted to CONUS and neighboring regions), with AIRS on the left and SNPP-CrIMSS on the right. The bottom left plot shows the SSDF fusion results. The bottom right plot shows the uncertainty estimates on the SSDF fusion results at the 1-sigma level. All units are degrees K.

387 Figures 2 and 3 provide maps representing one arbitrarily chosen day and night
 388 of the SSDF-AC product. For both the day and night cases, the top two plots show
 389 maps of the input satellite data ingested into the SSDF product, with AIRS on the left
 390 and SNPP-CrIMSS on the right; the bottom left plot shows the SSDF fusion results;
 391 and the bottom right plot shows the uncertainty estimates on the SSDF fusion results
 392 at the 1-sigma level. These sample maps demonstrate how our SSDF method fills
 393 in missing data in the input datasets by exploiting spatial correlations to provide a
 394 complete gap-filled, gridded product. Note that the estimated uncertainties are higher
 395 in regions that contain no observations, contain observations from only a single input
 396 dataset, or in which the two input datasets have relatively poor agreement.

397 3.2 Comparison of bias, standard deviation, and RMSE

398 We now turn to validation against withheld ISD reference data to quantify im-
 399 provement in the SSDF products. We emphasize that the ISD data used for validation
 400 were not the same as the ISD data used to estimate bias and variance in the course
 401 of creating the SSDF products, as we split the ISD matchup data into ‘training’ and
 402 ‘testing’ sets. We examine bias, standard deviation, and RMSE, calculated from the
 403 withheld matchups, of AIRS, CrIMSS, ERA5-Land, and the corresponding matched
 404 SSDF data. In what follows, we often analyze daytime and nighttime separately, as
 405 daytime and nighttime biases can differ significantly.

406 We first show maps of bias, RMSE, and standard deviation relative to the 1% of
 407 withheld (testing-only) ISD reference data, based on the matchups aggregated into the
 408 hexagonal bins. Figure 4 shows maps of bias (retrieval - ISD) for AIRS, CrIMSS, and
 409 SSDF, for the 2013-2020 period in total, and for day-only and night-only. Individual
 410 bias estimates for retrieval-ISM pairs are aggregated into 2-degree hexagonal cells.

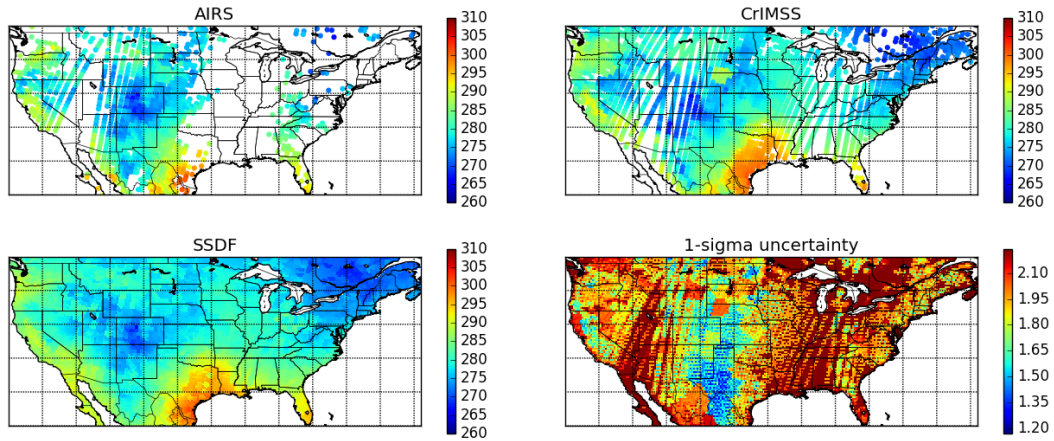


Figure 3: Same as Figure 2 but for night. All units are degrees K.

411 Overall, in the mean over CONUS and over the entire time period, SSDF provides
 412 a reduction in the magnitude of daytime bias of 1.7 K and 0.5 K relative to AIRS and
 413 CrIMMS, respectively. At night, SSDF is essentially unbiased in the mean over the
 414 domain and provides a reduction in the magnitude of bias of 1.5 K and 0.2 K relative
 415 to AIRS and CrIMMS, respectively.

416 AIRS shows a strong cold bias in daytime over the mountainous West, which
 417 is also present in CrIMSS, although less severe. AIRS shows a near-constant warm
 418 bias over the entire Eastern CONUS at night, while CrIMSS shows a sharp warm bias
 419 over small regions of the mountainous West at night. SSDF mitigates these biases
 420 (through the bias-correction procedure described above) and produces estimates with
 421 lower biases than either of its input satellite data sets over the domain.

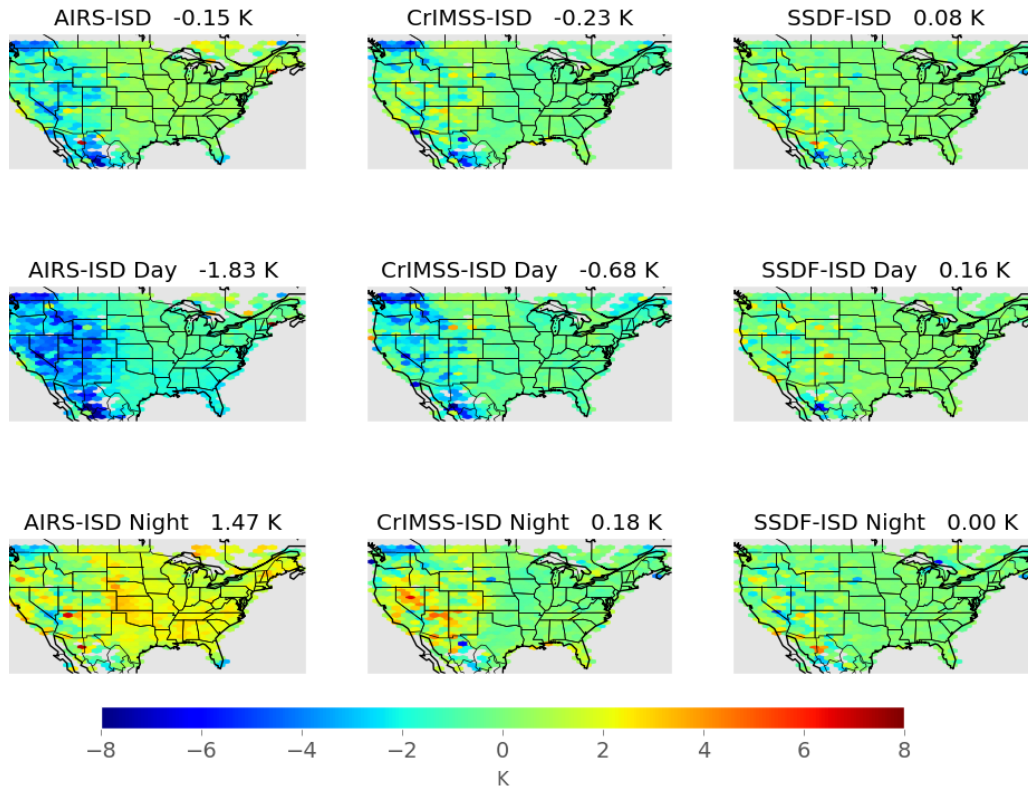


Figure 4: Maps of bias (retrieval - ISD) over the product period of 2013-2020, created against the withheld ISD test data, for AIRS (first column), CrIMSS-CLIMCAPS (second column) and SSDF (third column), for both day and night together (top row), for day only (second row) and for night only (third row). Individual bias estimates for retrieval-
ISD matchup pairs are aggregated over 2-degree hexagonal cells. The mean bias over CONUS for the entire time period is shown in the title for each map.

422 Figures 5 and 6 show maps of standard deviation and RMSE for AIRS, CrIMSS
 423 and SSDF, for the 2013-2020 period, and for daytime only and nighttime only. Stan-
 424 dard deviation and RMSE tell a similar story to that of bias. Overall, in the mean
 425 over CONUS and over the entire time period, SSDF provides a reduction in RMSE of
 426 35% and 15% compared to AIRS and CrIMSS, respectively.

427 CrIMSS has high RMSE over the mountainous West in both day and night,
 428 but low RMSE over the eastern two-thirds of the continent. Similarly, AIRS has
 429 relatively high RMSE over the entire domain, but especially over the mountainous
 430 West. Mountainous regions pose particular challenges for remote sensing of surface
 431 quantities, and of NSAT in particular, which can vary greatly depending on e.g., north-
 432 facing versus south-facing mountain surfaces. Furthermore, variations in topographic
 433 features between ISD stations and their matched remote sensing retrievals can lead
 434 to random errors, increasing RMSE and variance estimates. However, SSDF NSAT
 435 shows a clear decrease in bias over all regions, including in the mountainous western
 436 CONUS, although there is potential for improvement in the SSDF product over the
 437 West.

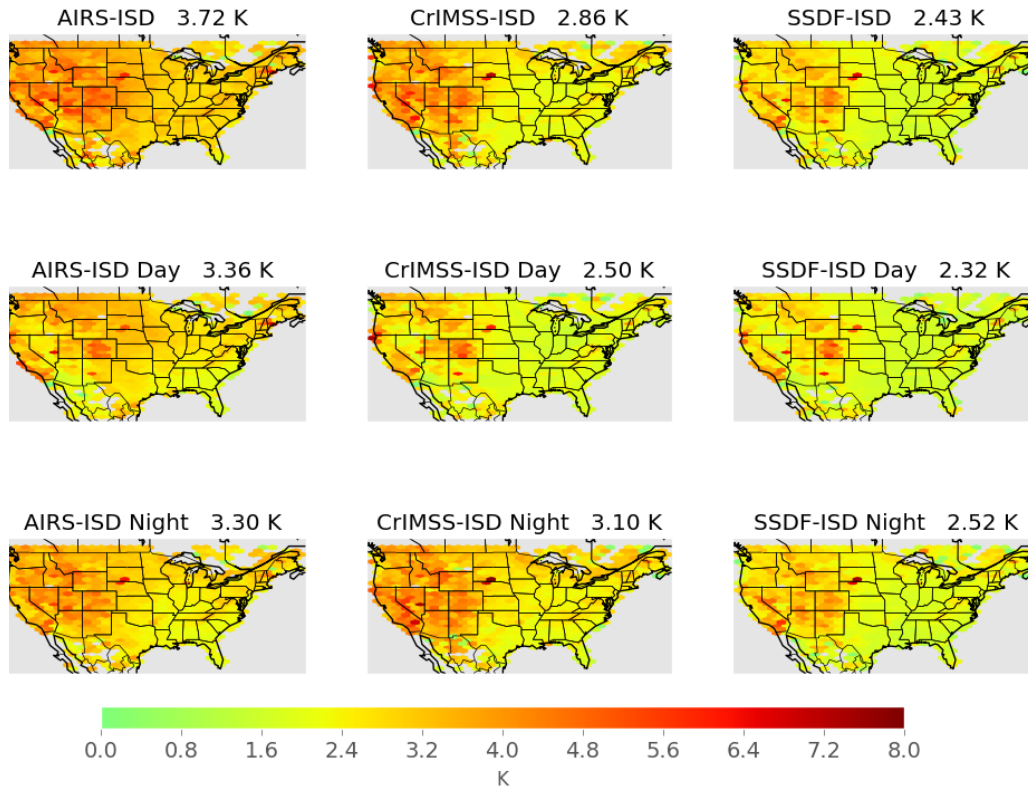


Figure 5: Standard deviation maps. The nine panels are similar to those in Figure 4 but for standard deviation.

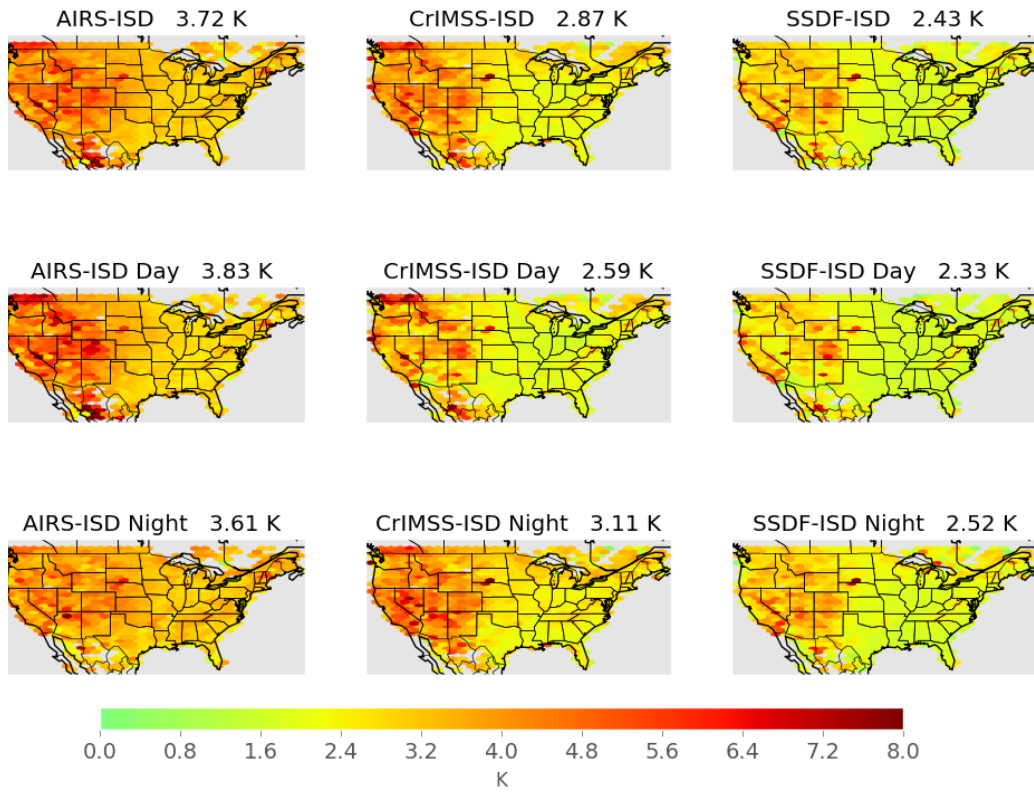


Figure 6: RMSE maps. The nine panels are similar to those in Figure 4 but for RMSE.

438 We repeated this analysis over CONUS and the 2013-2020 period for the SSDF-
 439 A product. We found similar improvements in bias, standard deviation, and RMSE.
 440 The mean bias of SSDF-A over the entire domain was -0.08 K for daytime only, and
 441 -0.03 K for nighttime only. The overall RMSE was 2.52 K, 4% higher than the overall
 442 RMSE of the SSDF-AC product.

443 Figure 7 shows histograms of the NSAT error (retrieval/reanalysis - ISD) for the
 444 year 2013, over CONUS only. The three comparison datasets (AIRS, CrIMSS, and
 445 ERA5-Land) were matched separately to SSDF outputs, to ensure that the SSDF
 446 product and each corresponding comparison dataset are considering the same scenes.
 447 The SSDF error histograms are symmetric with a single mode and peak at 0 for both
 448 day and night, which is consistent with the errors being unbiased relative to the ISD
 449 reference dataset. The AIRS histogram exhibits a cold bias during the day and a warm
 450 bias at night. CrIMSS has a similar day/night bias shift, but of a smaller magnitude. A
 451 cold bias over land, particularly at higher temperatures, has been previously noted for
 452 both input datasets (Yue et al., 2020, 2021), although there have been few validation
 453 studies (Ferguson & Wood, 2010; Sun et al., 2021). The SSDF product exhibits
 454 smaller mean biases and RMSEs than either input dataset. On average, over both
 455 input datasets, daytime and nighttime, SSDF decreases mean bias magnitude by 81%
 456 and mean RMSE by 23% relative to the input datasets.

457 Next, we examine the seasonality of bias and RMSE. Figure 8 shows the mean
 458 bias (retrieval/reanalysis - ISD) by month split into day/night to examine seasonality.
 459 There is a significant cold bias during the day for AIRS and CrIMSS that switches
 460 to a warm bias at night. During the day, AIRS has a smaller bias during winter
 461 months (Dec/Jan/Feb) and a larger bias during summer months (Jun/Jul/Aug). This
 462 is switched during nighttime where a larger warm bias is observed during winter and
 463 a smaller warm bias is observed during summer. These AIRS biases are of course also
 464 apparent in Figure 7. The SSDF product is relatively unbiased for both day and night.
 465 The SSDF bias magnitude is slightly larger during the day than night. From May to
 466 December, the SSDF product has a smaller bias at night than does ERA5-Land while
 467 during the day the reanalysis and the SSDF mean biases are of similar magnitude.

468 Figure 9 shows mean RMSE (retrieval/reanalysis - ISD) by month split by day/night,
 469 i.e., the mean RMSE values calculated in 2-degree spatial bins. RMSE is largest for
 470 AIRS, particularly during the day. Generally, RMSE is higher in winter and lower in
 471 summer. During the day, the ERA5-Land has the lowest RMSE. At night, the SSDF
 472 RMSE is comparable and sometimes lower than the ERA5-Land RMSE.

473 We next examine relative performance in hot and cold extremes. Figure 10 shows
 474 the mean bias (retrieval/reanalysis - ISD) by ISD percentile of the ISD matchups.
 475 The error bars indicate the standard error of the mean at the 95 percent confidence
 476 level. The lighter shade of every color is the matched SSDF corresponding to the
 477 comparison dataset. All retrievals and reanalysis do best in the mean state (25th to
 478 75th percentile). At the extremes, each of the datasets being compared to ISD have
 479 warm biases for low values (1st through the 15th percentile) and cold biases for high
 480 values (85th through the 99th); in other words, all of the datasets understate cold
 481 or warm extremes represented in the ISD. The SSDF product captures the extremes
 482 better than both the AIRS and CrIMSS inputs. However, the reanalysis generally
 483 does best, having the smallest bias regardless of percentile, and is better at capturing
 484 the extremes.

485 We next examine performance at extremely high elevations. Figure 11 shows
 486 mean biases (retrieval/reanalysis - ISD) aggregated by ISD elevation. At around 2500
 487 meters, mean biases increase with elevation in the SSDF product, AIRS, CrIMSS, and
 488 reanalysis. Daytime mean biases at these high elevations are larger in SSDF, although

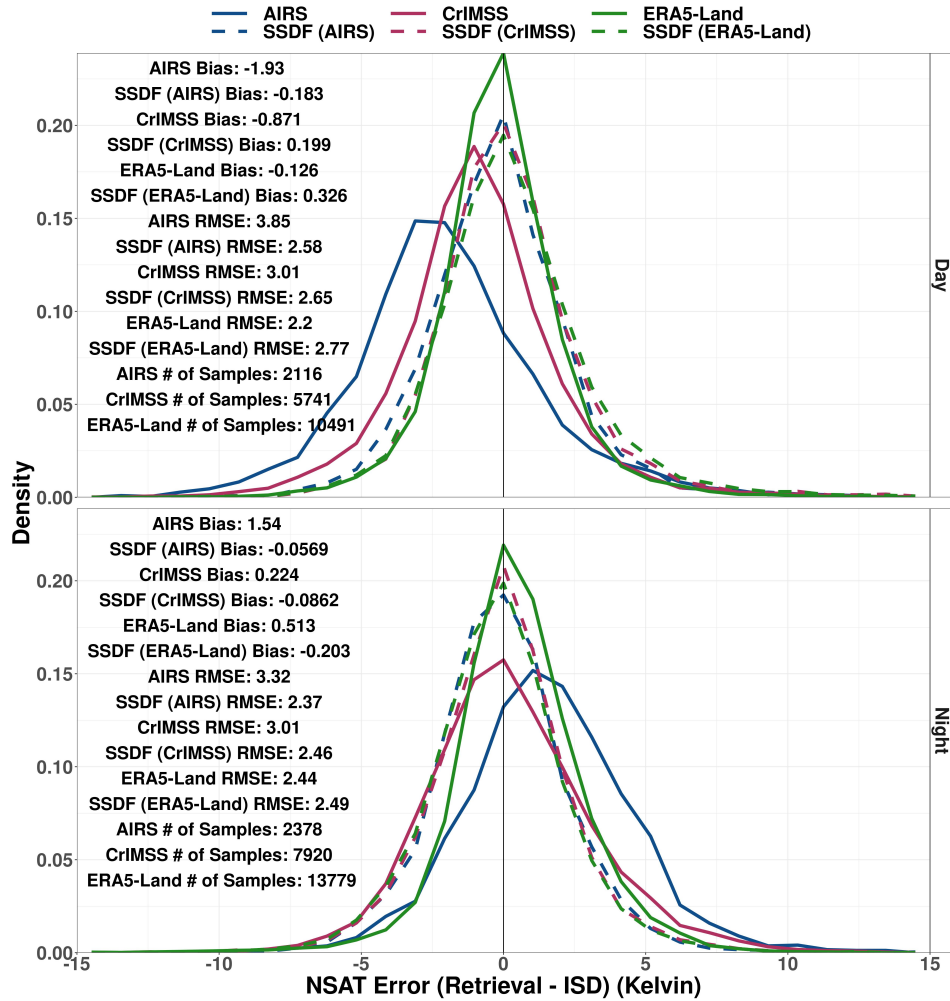


Figure 7: Histograms of errors for day (top) and night (bottom) for 2013 over CONUS, for AIRS (blue), CrIMSS (red) and ERA5-Land (green). The dashed line is the SSDF-AC subset matched to the other datasets. Mean statistics of bias, RMSE, and the number of samples are provided.

489 we note that the sample size is small. At night, SSDF shows lower mean biases than
 490 AIRS, CrIMSS, or ERA5-Land at high elevations.

491 In order to increase the sample size for high-elevation cases, Figure 12 shows
 492 the mean biases aggregated by ISD elevation for elevations higher than 2000 meters
 493 over the period 2012-2020. During the day, the SSDF bias exceeds AIRS and CrIMSS,
 494 consistent with Figure 11. We hypothesize that this excess bias in SSDF for a very small
 495 number of data points at very high elevations is caused by the bulk-binning method
 496 for bias estimation. As Figure 11 shows, both remote sensing datasets exhibit a cold
 497 bias during the daytime at lower elevations. Because the two-degree hexagonal bins for
 498 bias estimation are dominated by lower elevations (as the problematic high elevations
 499 are high mountain surfaces), and because both remote sensing dataset biases switch
 500 signs from cold bias to warm bias at approximately 2500 m, the cold bias correction
 501 calculated from the bulk bins ends up exacerbating the warm bias from the input
 502 datasets at the highest elevations. In a future version of SSDF, we will improve the

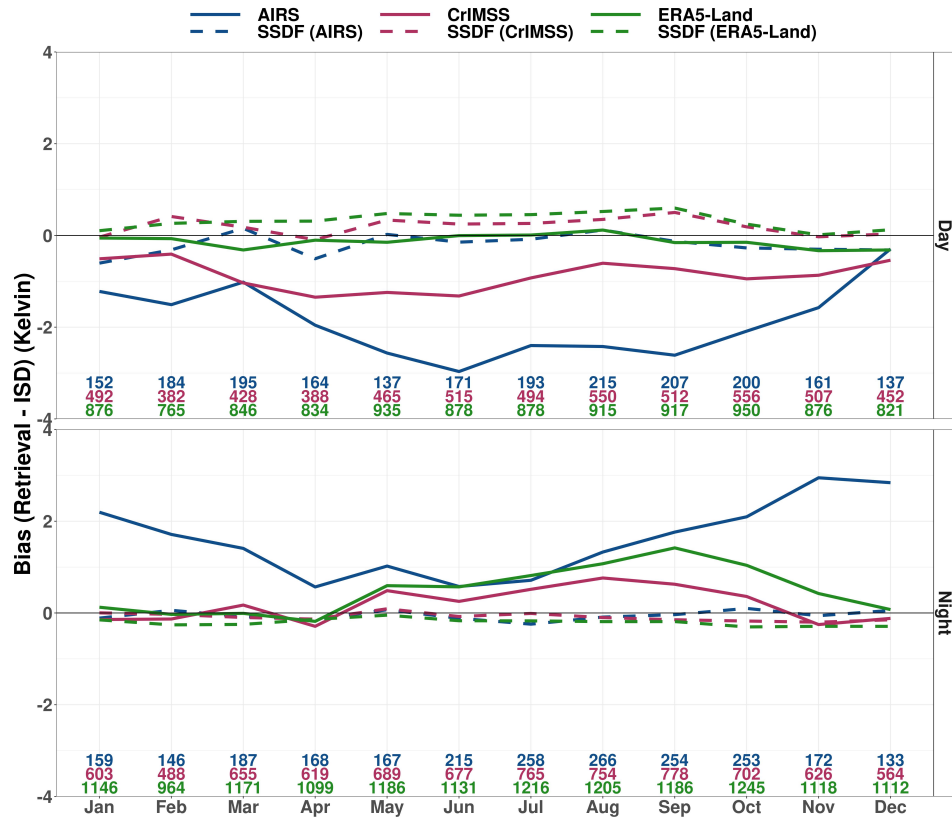


Figure 8: Mean bias as a function of month for day (top) and night (bottom) for 2013 over CONUS. Numbers at the bottom indicate the number of data points, and are color-coded according to dataset.

503 bias estimation of the input datasets, which could mitigate or eliminate this bias at
 504 the small number of estimates elevations above 2500 m.



Figure 9: Mean RMSE as a function of month for day (top) and night (bottom) for 2013 over CONUS. Numbers at the bottom indicate the number of data points, and are color-coded according to dataset.

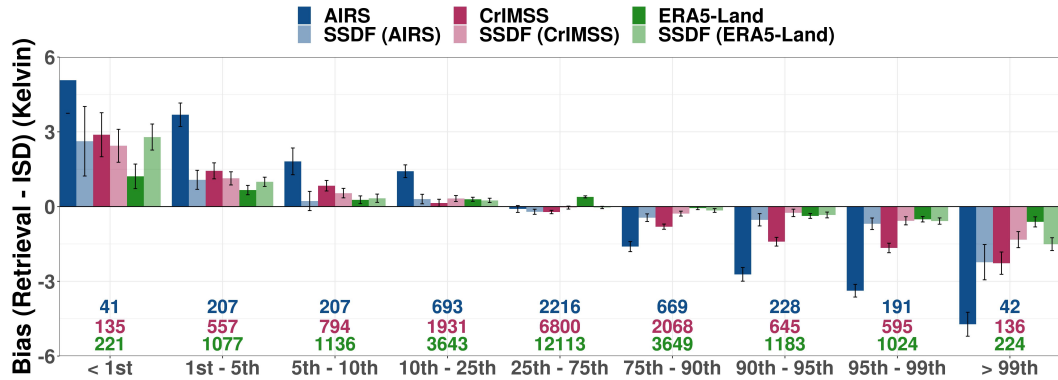


Figure 10: Mean biases as a function of ISD percentile for 2013 over CONUS. Numbers at the bottom indicate the number of data points, and are color-coded according to dataset.

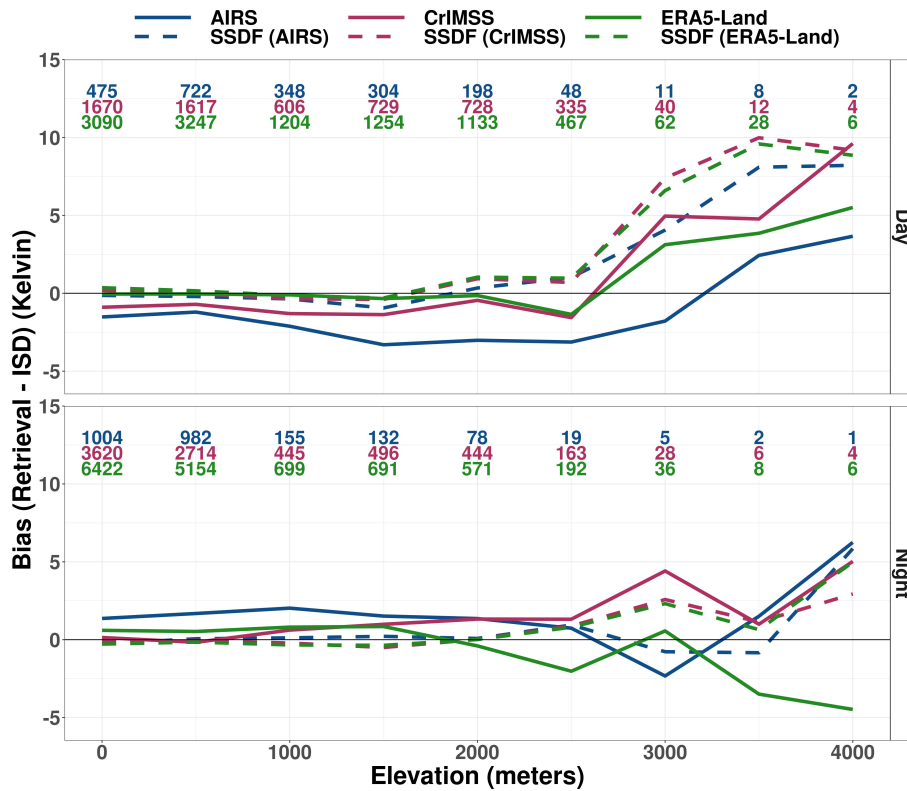


Figure 11: Mean biases as a function of ISD elevation for day (top) and night (bottom) for 2013 over CONUS. Numbers at the top indicate the number of data points, and are color-coded according to dataset.

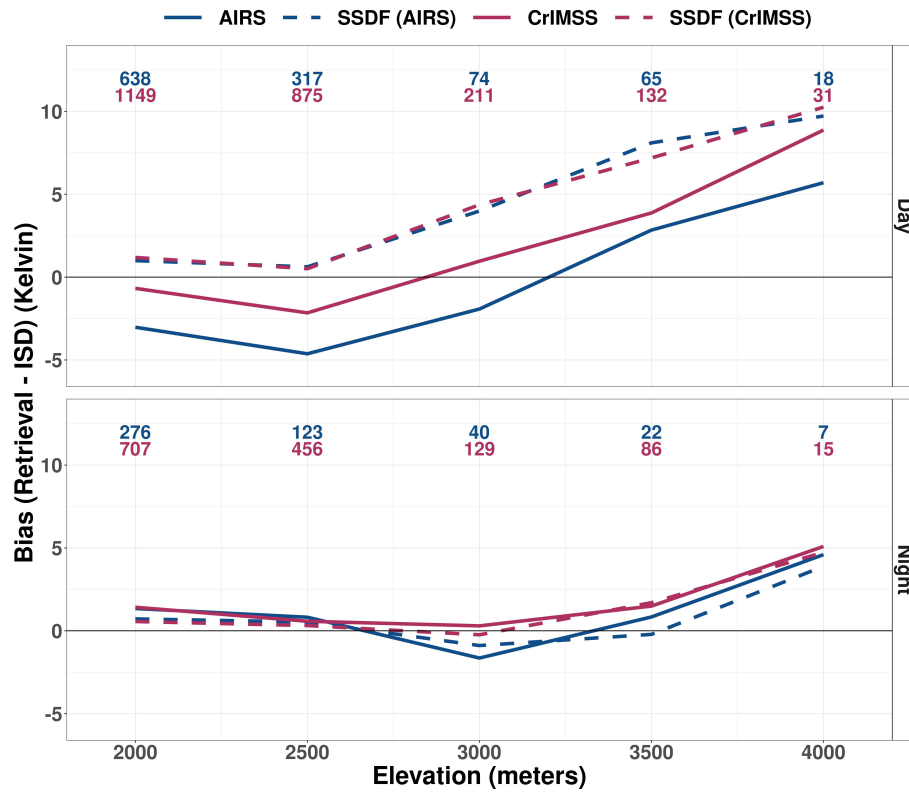


Figure 12: Mean biases as a function of ISD elevation for day (top) and night (bottom) over CONUS from 2012-2020 for AIRS, CrIMSS, and SSDF. Numbers at the top indicate the number of data points, and are color-coded according to dataset.

505

3.3 Comparison of uncertainty estimates

506

507

508

509

510

511

512

513

The SSDF algorithm provides a mean (prediction/estimate) and standard deviation (uncertainty) of the conditional distribution of true NSAT, given the available inputs; this distribution is termed the predictive distribution. In what follows, this is a Gaussian distribution, centered at the SSDF estimate. This information can be used to construct prediction intervals for the true NSAT. Here we provide a summary and probabilistic assessment of the SSDF predictive distribution along with related information from the AIRS V7 and CrIMSS-CLIMCAPS V2 products. In the notation that follows, we use the subscript i in place of the areal unit notation B_i .

514

515

516

517

518

519

520

521

522

523

524

- In addition to each SSDF NSAT estimate, \hat{Y}_i , the algorithm also provides the conditional standard deviation of the predictive distribution, denoted $\hat{\sigma}_{\hat{Y},i}$.
- The AIRS V7 NSAT retrieval, $Z_{1,i}$, is accompanied by a corresponding uncertainty estimate, denoted $\hat{\sigma}_{Z,1,i}$ (Susskind et al., 2014). This estimate results from a regression model for predicting the absolute retrieval error given several predictors available from the retrieval.
- The CrIMSS-CLIMCAPS V2 retrieval, $Z_{2,i}$, also has a corresponding uncertainty estimate, denoted $\hat{\sigma}_{Z,2,i}$ (N. Smith & Barnet, 2020). This estimate results from a linear approximation of the posterior standard deviation of the true state given the observed radiances for a single footprint and is an output of the optimal estimation (OE) approach used in CLIMCAPS.

525

526

527

528

529

530

Figure 13 shows histograms of these uncertainty estimates: $\hat{\sigma}_{Z,1}$, $\hat{\sigma}_{Z,2}$, and $\hat{\sigma}_{\hat{Y}}$ across the CONUS data record. The solid line shows uncertainty estimates from AIRS (blue) and CrIMSS (red) while the dashed shows the corresponding matched SSDF uncertainty estimates. CrIMSS has a peak around 1.2 K with a narrow distribution; AIRS V7 has a peak between 1.5 and 2 K with a wide distribution. SSDF uncertainty histograms peak around 2 K.

531

532

533

534

These uncertainty estimates are properties of distributions, whereas we define error e_i as a realization of a random variable that represents the difference between an estimate and the true state. For example, the error for SSDF is $e_{\hat{y},i} = \hat{Y}_i - Y_i$, where Y_i is the ISD validation for colocation i . If the predictive distribution is assumed to be Gaussian, the empirical coverage of intervals of the form

$$\hat{Y}_i \pm c \hat{\sigma}_{\hat{Y},i},$$

531

532

533

534

can be assessed for the ISD matchups. In the case of an unbiased estimate, “well-calibrated” uncertainty estimates, and a Gaussian distribution; intervals with $c = 1$ should cover the true state Y_i about 68% of the time, and about 95% of the time for $c = 2$.

535

536

537

538

539

540

541

542

543

544

Figure 14 shows scatterplots of the joint distribution of the uncertainty estimate (x-axis) and the observed error (retrieval-*ISD*). There are many cases for AIRS and CrIMSS where the uncertainty estimate grossly underestimates the true error; over 15% of the time for both datasets and for day and night, the true error is more than three times greater than the uncertainty estimate. However, this occurs about 3% of the time with SSDF in the day and fewer than 5% of the time at night. Overall, the CrIMSS uncertainty estimates are distributed too narrowly, and with a peak too low, to capture the true error. The AIRS uncertainty estimates also peak at a value below the peak of the error distribution, although the uncertainty estimate distribution is much wider, including a very long tail of high uncertainty estimates.

545

546

547

In general, SSDF uncertainty estimates are consistent with statistical expectations under Gaussian assumptions. For example, one would expect one-sigma uncertainty estimates to cover a standard error distribution 68% of the time, and we see

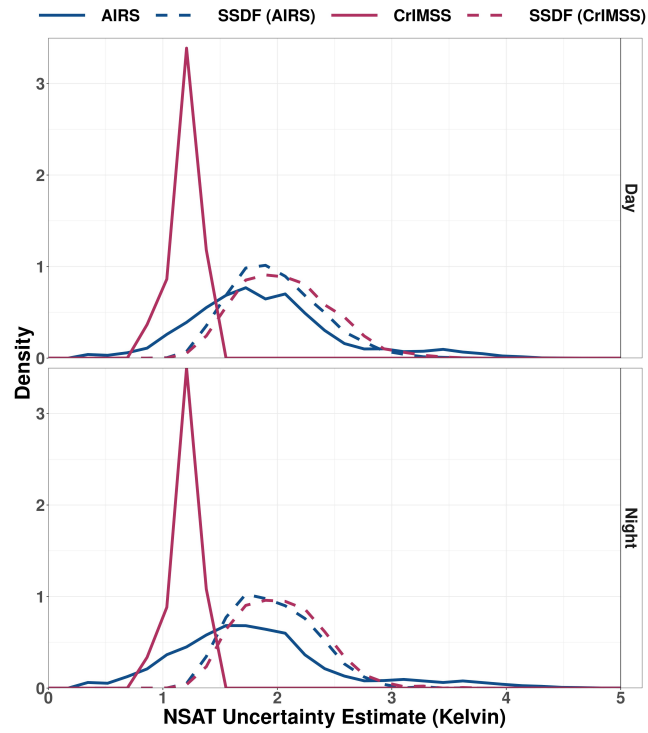


Figure 13: Histograms of uncertainty estimates for day (top) and night (bottom) for 2013 over CONUS.

548 that the SSDF uncertainty estimates do so roughly 65% of the time in daytime. Simi-
 549 larly, one would expect the estimates to cover 95% and over 99% at the 2- and 3-sigma
 550 levels, with SSDF covering about 90% and 97% during daytime.

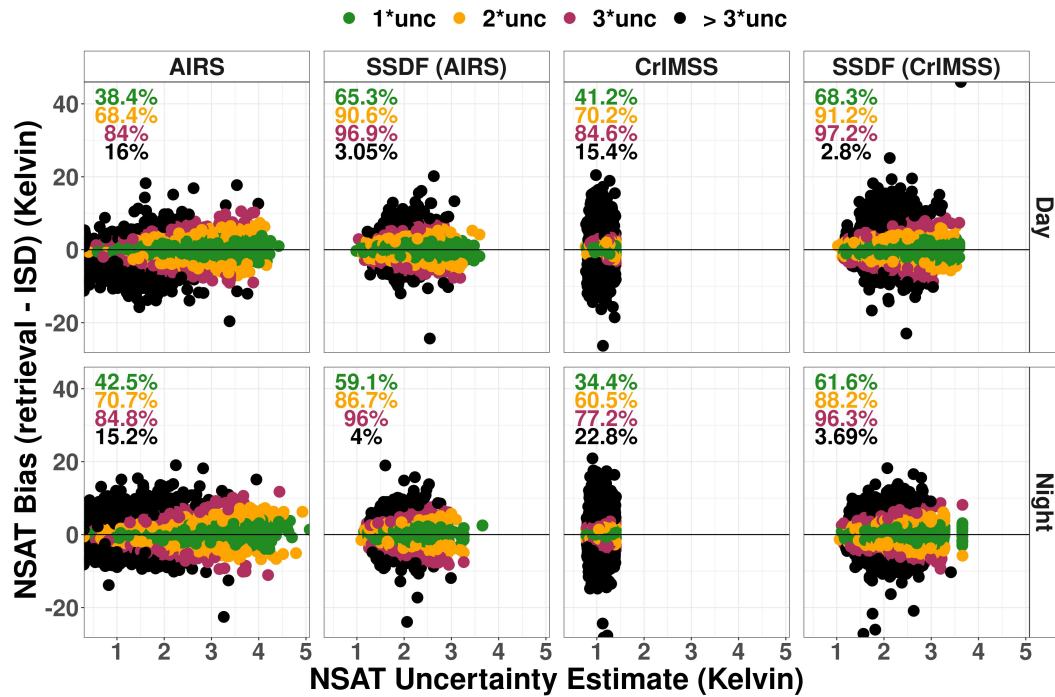


Figure 14: Observed errors (retrieval - ISD) versus uncertainty estimates for day (top) and night (bottom) for 2013 over CONUS. The colors show whether the range of each observed error was within the uncertainty bound, as described in the text: 1×uncertainty (green, should cover the true state about 68% of the time), 2×uncertainty (orange, should cover the true state about 95% of the time), 3×uncertainty (red, should cover the true state about 99% of the time) or > 3×uncertainty (black).

551

3.4 Empirical distribution consistency

552

553

554

555

556

557

558

559

560

The ISD record provides a sample of the empirical distribution of NSAT over CONUS. Here, we assess the relative consistency of the SSDF empirical distribution versus the other products against the ISD reference distribution. Figure 15 shows an example of the empirical cumulative distribution (ECDF) for the ISD (pink) and AIRS (blue). While it is almost certainly the case that the products' ECDFs deviate from the ISD reference distribution in some subtle ways, we evaluate their relative consistency with ISD through a series of hypothesis tests. Figure 16 shows the difference between the ECDF of the retrieval/reanalysis to the ECDF of ISD. The AIRS ECDF has the largest difference to the ISD ECDF, particularly during the Day.

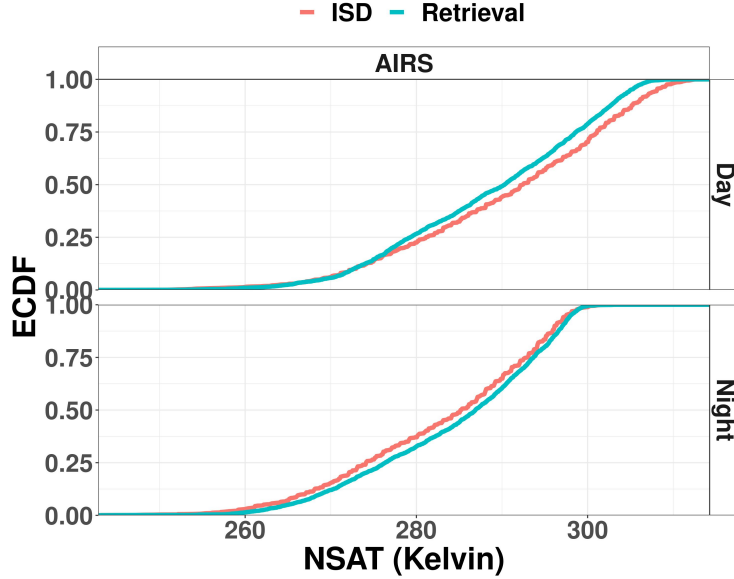


Figure 15: ECDF for AIRS (blue) and ISD (pink) for day (top) and night (bottom) for 2013 over CONUS.

561

562

563

564

565

566

567

568

The SSDF estimates are tested against each of the other products (AIRS, CrIMSS, ERA5-Land) for night and day conditions. Each assessment is carried out using a randomization or resampling test (Wilks, 2006). For this test, the null hypothesis is that the empirical distributions of SSDF and the comparison product deviate equally from the ISD reference distribution. The alternative hypothesis is that either SSDF or the comparison product have an empirical distribution that is closer to the ISD reference distribution. For this procedure, the test statistic is computed as the difference in two-sample Kolmogorov-Smirnov (KS) statistics for the products versus ISD.

For each instance of the test, we have a collection of matched triples $\{\hat{\mathbf{Y}}, \mathbf{Z}_k, \mathbf{Y}\}$; where $\hat{\mathbf{Y}} \equiv \{\hat{Y}_i\}; i = 1, \dots, n$ are the SSDF estimates, $\mathbf{Z}_k \equiv \{Z_{k,i}\}; i = 1, \dots, n$ are the comparison products, and $\mathbf{Y} \equiv \{Y_i\}; i = 1, \dots, n$ are the ISD NSAT. As above, $k = 1$ for AIRS, $k = 2$ for CrIMSS, and here $k = 3$ for ERA5-Land. Then, test k has a test statistic

$$\gamma_k = \delta(\hat{\mathbf{Y}}, \mathbf{Y}) - \delta(\mathbf{Z}_k, \mathbf{Y}),$$

569

570

571

572

where δ is the traditional two-sample KS statistic. The KS statistic is the maximum difference in the two ECDFs being compared. Thus, the test statistic γ_k for the current test is a *difference* of ECDF deviations. A negative value is an indication that the SSDF distribution is closer to ISD than the comparison product.

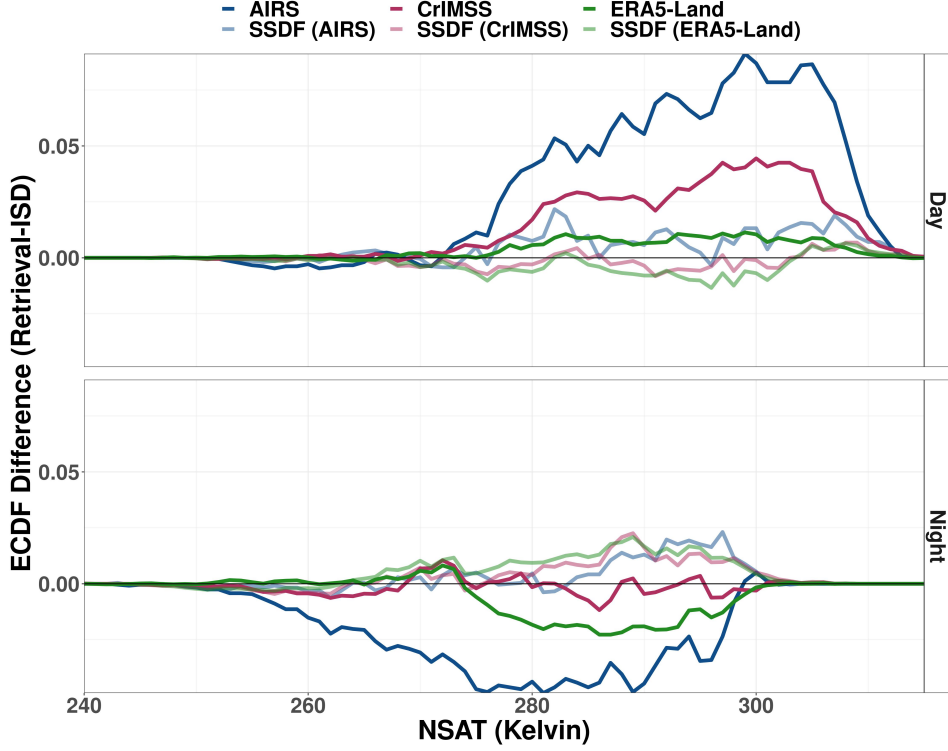


Figure 16: The ECDF difference between the retrieval/reanalysis and the ISD color coded for day (top) and night (bottom) for 2013 over CONUS.

573 The distribution of the test statistic under the null hypothesis can be estab-
 574 lished through a resampling procedure. The procedure should preserve the inherent
 575 dependence of the matched triples, but the assignment of the two comparison groups
 576 can be shuffled randomly. A null distribution is generated by repeating these steps
 577 $m = 1, \dots, M$ times:

- 578 1. Define shuffled data vectors $\mathbf{W}_{m,1}$ and $\mathbf{W}_{m,2}$.
- 579 2. For each validation matchup ($i = 1, \dots, n_k$), assign $W_{i,m,1} = \hat{Y}_i$ and $W_{i,m,2} =$
 580 $Z_{k,i}$ with probability 0.5; otherwise assign $W_{i,m,1} = Z_{k,i}$ and $W_{i,m,2} = \hat{Y}_i$. This
 581 effectively shuffles the labels for SSDF and the comparison product for each
 582 matchup.
3. Compute the test statistic for the randomized samples,

$$\gamma_{0,m,k} = \delta(\mathbf{W}_{m,1}, \mathbf{Y}) - \delta(\mathbf{W}_{m,2}, \mathbf{Y}),$$

The distribution of $\gamma_{0,m,k}$ provides the null distribution of the test statistic for each test. Figure 17 displays the test statistics γ_k along with density plots of the null distributions of test statistics $\gamma_{0,m,k}$ for $M = 20,000$ resampled datasets for each test. A two-sided p -value can be computed for each test as

$$p_k = \frac{1}{M} \sum_{m=1}^M I_\gamma(|\gamma_{0,m,k}| > |\gamma_k|),$$

583 where I_γ is an indicator function.

584 The p -values for each of the resampling tests of SSDF versus other products are
 585 displayed as text in Figure 17. All tests, except the night comparison of SSDF and
 586 CrIMSS, yield p -values of 0, indicating a significant difference in consistency with the
 587 ISD reference distribution. These results can also be seen visually as the observed test
 588 statistics γ_k , shown as vertical lines, lie well outside the corresponding null distribu-
 589 tions. The tests indicate SSDF is more consistent with ISD than AIRS for both day
 590 and night conditions, as well as a favorable result for SSDF versus CrIMSS for day and
 591 versus ERA5-Land at night. The positive test statistic for SSDF versus ERA5-Land
 592 during the day indicates the reanalysis is more consistent with ISD in this case.

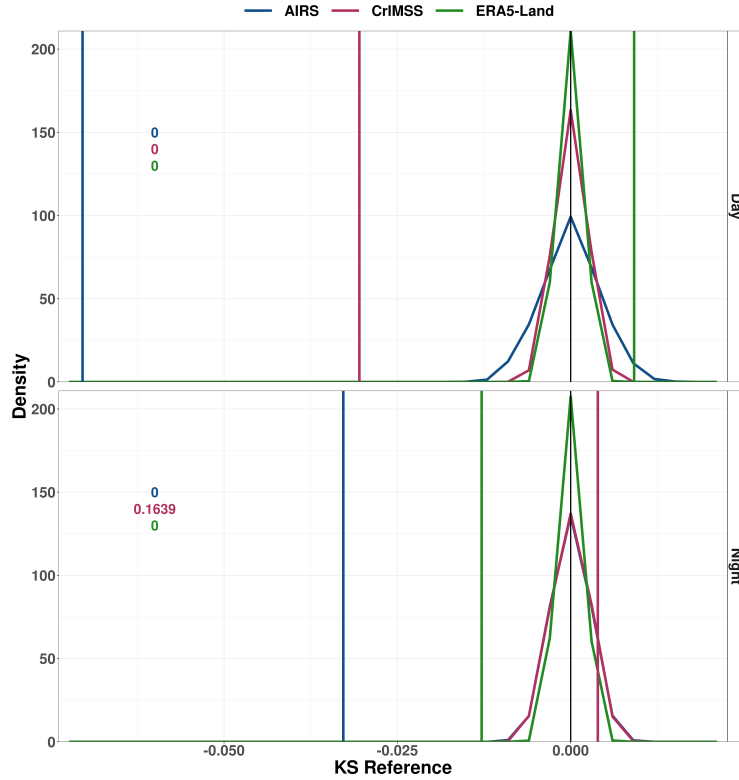


Figure 17: Histogram of the KS statistic for AIRS (blue), CrIMSS (maroon) and ERA5-Land (green), for day (top) and night (bottom) for 2013 over CONUS. The corresponding p -value is color-coded on the left side.

593 3.5 Stationarity

594 Long-term stationarity is a key characteristic for creating long, stable, multi-
 595 instrument Earth science data records. To assess long-term bias stationarity, we cal-
 596 culated mean annual biases over CONUS relative to the withheld ISD data for the two
 597 input datasets and SSDF. Figure 18 shows the annual mean bias for both the input
 598 datasets, as well as for SSDF-AC and SSDF-A. Shading shows two standard deviations
 599 of these annual bias estimates. We include full years only.

600 SSDF reduces the mean magnitude, the variance, and the trend in these annual
 601 bias time series, with the biases estimated relative to the ISD reference dataset. For
 602 AIRS and SSDF-A matched to AIRS from 2003-2020, the overall means of the annual

603 bias time series were -0.10 K and -0.035 K and the standard deviations of the annual
 604 bias time series were 0.17 K and 0.035 K.

605 We estimated trends and trend uncertainties using the nonparametric technique
 606 called Thiel Sens Slope (Sen, 1968) which is based on the medians. We used the Mann-
 607 Kendall test to assess statistical significance (Mann, 1945; Kendall, 1948). Trends
 608 for AIRS and SSDF-A were -0.01 K/yr (p -value 0.08) and -0.003 K/yr (p -value 6e-
 609 8), respectively, over the 2003-2020 period. The AIRS trend was less statistically
 610 significant due to the high standard deviation in the time series.

611 For CrIMSS and SSDF-AC from 2013-2020, the overall means of the annual bias
 612 time series were -0.23 K and 0.076 K and the standard deviations of the annual bias
 613 time series were 0.059 K and 0.024 K respectively. Trends were 0.009 K/yr and -0.0007
 614 K/yr, respectively; neither trend is statistically significant, with p -values of 0.6 and
 615 0.8, respectively.

616 The annual mean biases also reveal a shift of about 0.1 K between the SSDF-AC
 617 and SSDF-A products. This shift is small compared to the biases in the input remote
 618 sensing datasets, but it is undesirable. We hypothesize that it could be an artifact
 619 of the bulk-binning bias estimation procedure, and subsequent bias correction, due to
 620 differing systematic error characteristics in the two input datasets. Future versions of
 621 SSDF will use improved uncertainty quantification methods to estimate input dataset
 622 biases, which could mitigate or eliminate this small difference mean bias between SSDF
 623 products created from different combinations of input datasets.

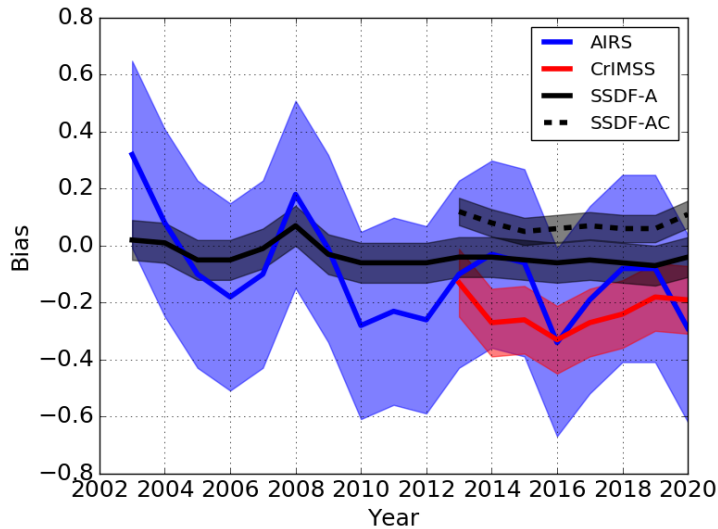


Figure 18: Annual mean bias for each year of the data record, for the SSDF product and each of the two remote sensing input products, relative to the withheld ISD data. Shading shows two standard deviations of these annual bias estimates. SSDF-A refers to the AIRS-only SSDF product; SSDF-AC refers to the SSDF product created from both the AIRS and SNPP-CLIMCAPS input datasets.

624 Figure 19 shows the histogram of the SSDF uncertainty estimates for 2011 (black)
 625 and 2013 (red). The mean uncertainty is provided as text. The histograms are compar-
 626 able, although the SSDF-AC product in 2013 has mean uncertainties that are 4%
 627 lower on average than the SSDF-A product in 2011. This is to be expected as the
 628 additional information from CrIMSS provides greater certainty for SSDF.

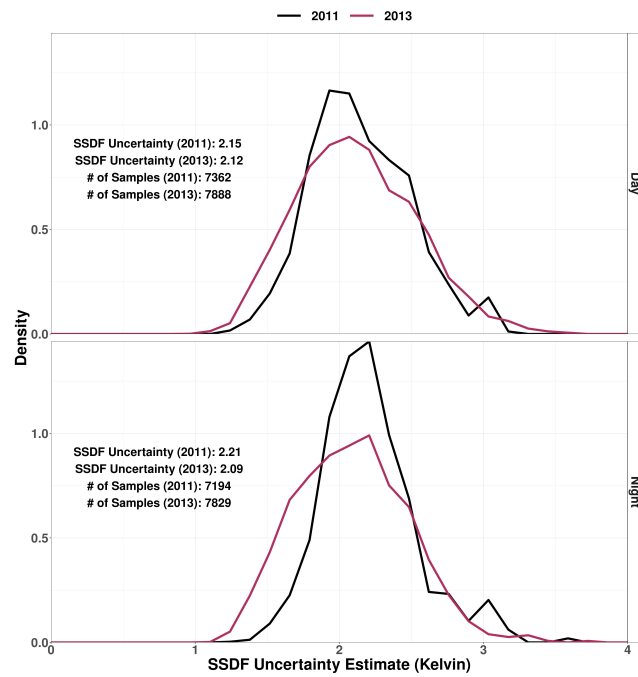


Figure 19: SSDF uncertainty histogram for 2011 (black) and 2013 (red) aggregated by day (top) and night(bottom). Summary statistics of mean SSDF uncertainty are provided as text on the upper left.

4 Discussion and conclusion

We have produced a new fused NSAT product over CONUS, from November 2012 through December 2020, using Spatial Statistical Data Fusion of Aqua-AIRS V7 and SNPP-CrIMSS CLIMCAPS V2 L2 NSAT datasets. Remote sensing data provides information to span the spatial domain, in situ data provides the information to correct the remote sensing data, and SSDF provides the means to fuse them into an improved dataset.

The SSDF NSAT product could be used for applications over CONUS that require NSAT data and that would benefit from the improvements we have demonstrated here from a detailed validation using withheld ISD data as a reference dataset. The SSDF method generates a fused gridded product that has no missing data; has improved accuracy and precision relative to the input satellite datasets; and includes uncertainty estimates that are more consistent with the observed errors relative to the ISD reference. The NSAT SSDF pilot product is comparable in precision and accuracy to the state-of-the-art ERA5-Land reanalysis, but unlike reanalysis it does not involve dynamical weather modeling, only spatial covariance modeling. Furthermore, unlike reanalysis it could in the future support a near-real-time version for operational applications.

SSDF is a general method and can be applied to one or more L2 datasets, so long as each dataset estimates the same observable. For example, fusion of Aqua-AIRS and SNPP-CrIMSS estimates of NSAT works because both satellites estimate NSAT at approximately 1:30 and 13:30 local solar time. However, it would not make sense to directly fuse NSAT estimates from Infrared Atmospheric Sounding Interferometer (IASI) instruments on the MetOp satellites with the Aqua and SNPP datasets, as the MetOp satellites pass over at approximately 9:30 and 21:30 local solar time, when NSAT is at different points of the diurnal cycle. On the other hand, the details of instruments used to make the input datasets, and their spatial footprints and sampling, are immaterial. For example, it would be possible to fuse NSAT derived from the Visible Infrared Imaging Radiometer Suite (VIIRS) land surface temperature (LST) product via (for example) regression modeling (Good, 2015), since such a LST-derived NSAT product would also sample at approximately 1:30 and 13:30 local solar time. SSDF could be applied across a wide range of observables estimated as L2 satellite datasets, such as atmospheric composition, water vapor profiles, or vapor pressure deficit (the difference between the water vapour pressure and the saturation water vapour pressure). Bias and variance estimates of the input datasets are required, and we emphasize that the quality of the SSDF product depends on the quality of those error estimates.

Our plans for future work include improving the bias and variance estimation using simulation-based uncertainty quantification (Hobbs et al., 2017; Braverman et al., 2021). Simulation-based uncertainty quantification has the potential to further improve the overall quality of the SSDF product. It could also mitigate or eliminate the two issues our validation has uncovered, namely (1) increased bias at a small number of data points at elevations in excess of 2500 m, and (2) a ~ 0.1 K shift in annual mean bias between the SSDF-AC and SSDF-A (AIRS-only) versions.

We also plan to create an NSAT SSDF product over global land areas, create a high spatial resolution NSAT SSDF product by including high spatial resolution input NSAT datasets in the fusion, and apply the SSDF method to other hyperspectral surface products, starting with near-surface specific humidity.

Open Research

The SSDF NSAT datasets described in this paper are available from the NASA GES DISC repository at <https://doi.org/10.5067/CPXNAPA2WSQ8> (SSDF-AC) and <https://doi.org/10.5067/8AE9Y5TSXFX4> (SSDF-A).

Publicly available data were obtained from the NASA Atmospheric Infrared Sounder and the Suomi-NPP projects, the NOAA Integrated Surface Database, and the European Centre for Medium-Range Weather Forecasts reanalysis.

Aqua AIRS V7 is available from the NASA GES DISC repository (AIRS Project, 2019). The retrieved surface air temperature (TSurfAir), the corresponding error estimate for TSurfAir (TSurfAirErr), and the corresponding quality flag (QC) (TSurfAir_QC) were obtained for the standard IR-only product.

SNPP-CrIMSS-CLIMCAPS V2 is available from the NASA GES DISC repository (Barnet, 2019). Near surface temperature (surf_air_temp), the corresponding QC flag (surf_air_temp_qc), and the corresponding error estimate (surf_air_temp_err) were obtained from the NSR product.

NOAA ISD NSAT data is available using the rnoaa R package.

ECMWF ERA5-Land gridded hourly 2 m temperature means are available from the Copernicus Climate Change Service (C3S) Climate Data Store (Copernicus 2017).

Acknowledgments

The research was carried out at the Jet Propulsion Laboratory, California Institute of Technology, under a contract with the National Aeronautics and Space Administration (80NM0018D0004). We thank Evan Fishbein, Evan Manning, Erik Fetzer, and Bjorn Lambrigtsen for helpful discussions. ©2022

Appendix A Matchups and bias estimation

In this appendix, we will elaborate in detail our procedure for matching between ISD and the instruments' observations, and the consequent bias estimation process. For clarity, we establish the following notation. Let \mathbf{s} , \mathbf{u} , and \mathbf{v} be latitude-longitude locations; e.g., $\mathbf{s} = (lat, lon)$. On a given day (or night) let $Z^k(\mathbf{u})$ be the value of the k -th instrument's near-surface temperature retrieval centered at \mathbf{u} . and focus on a single ISD station at location \mathbf{s} during a single period. Let $t_1^I(\mathbf{s}), \dots, t_M^I(\mathbf{s})$ be the times at which observations are acquired at this station during the period. These time points may be irregularly spaced, and M can change from station to station. The ISD measurements are $Z^I(\mathbf{s}, Z_m^I(\mathbf{s}))$, $m = 1, \dots, M$.

Let $t^k(\mathbf{u})$ be the acquisition times associated with the k -th instrument's footprints centered at location \mathbf{u} . In principle, \mathbf{u} ranges over all footprint locations for the appropriate instrument during the entire period, but in practice these locations are grouped by granules. We denote granule number during the current period by $g = 1, \dots, 120$, and the set of footprints belonging to granule g by \mathcal{G}_g^k . The time associated with \mathcal{G}_g^k is τ_g^k . To ease the computational burden, \mathbf{u} ranges only over locations in the single granule with time that is closest to $t_m^I(\mathbf{s})$.

A matchup associates the location and time of an ISD value, $(\mathbf{s}, t^I(\mathbf{s}))$, with the location and time of the k -th instrument's footprint in the period: $(\mathbf{u}^*, t^k(\mathbf{u}^*))$. The *matchup function* is,

$$\begin{aligned} \mathbb{M}^k(\mathbf{s}, t_m^I(\mathbf{s})) &= (\mathbf{u}^*, t^k(\mathbf{u}^*)), \\ \mathbf{u}^* &= \underset{\mathbf{u}}{\operatorname{argmin}} \left\{ \|\mathbf{u} - \mathbf{s}\|, \mathbf{u} \in (\mathcal{G}_{g^*}^k \cap \mathcal{U}^{time} \cap \mathcal{U}^{space}) \right\}, \\ g^* &= \underset{g}{\operatorname{argmin}} \left\{ |\tau_g^k - t_m^I(\mathbf{s})| \right\}, \\ \mathcal{U}^{time} &= \left\{ \mathbf{u} : |t^k(\mathbf{u}) - t_m^I(\mathbf{s})| \leq 1 \text{ hour} \right\}, \quad \mathcal{U}^{space} = \left\{ \mathbf{u} : \|\mathbf{u} - \mathbf{s}\| \leq 100 \text{ km} \right\}. \end{aligned}$$

Note that, for a given instrument and period, there will only be one granule that satisfies the criterion provided by g^* .

For a given ISD station (indexed by location \mathbf{s}) in the current period, p , we create the sets of matchup values for the k -th instrument as follows,

$$\mathcal{A}^k(p, \mathbf{s}) = \left\{ Z^I(\mathbf{s}, t_m^I(\mathbf{s})), Z^k(\mathbb{M}^k(\mathbf{s}, t_m^I(\mathbf{s}))) \right\}_{m=1}^{M(p, \mathbf{s})}$$

for all ISD time points at \mathbf{s} indexed by $m = 1, \dots, M(p, \mathbf{s})$. p is identified by a date and a mode (day/night) indicator, e.g., $p = (d, j) = (2013-01-01, \text{day})$. $M(p, \mathbf{s})$ is the number of ISD station values in period p at location \mathbf{s} . There is at most one AIRS and one CrIMSS footprint associated with each station-time, but the same footprint can be associated with more than one station-time. Thus, $\mathcal{A}^k(p, \mathbf{s})$ may contain multiple elements if there is more than one ISD measurement during period p at location \mathbf{s} . They may also be empty if there are no matching AIRS or CrIMSS footprints.

After creating $\mathcal{A}^k(p, \mathbf{s})$ for all periods and ISD locations, we create supersets of matchup value pairs by combining across three-day moving windows, by mode:

$$\mathcal{A}^{kj}(d, \mathbf{s}) = \mathcal{A}^k(d-1, j, \mathbf{s}) \cup \mathcal{A}^k(d, j, \mathbf{s}) \cup \mathcal{A}^k(d+1, j, \mathbf{s}), \quad \mathcal{A}^{kj}(d) = \bigcup_{\mathbf{s}} \mathcal{A}^{kj}(d, \mathbf{s}).$$

$j \in \{\text{day, night}\}$. We chose the three-day time window after experimenting with shorter and longer windows. Shorter windows did not provide adequate sample sizes while longer windows failed to capture weather-related changes. Ideally, window duration would be as short as possible since longer time windows result in larger variance estimates in the fused data, relative to withheld ISD data.

The final step before actually computing estimated bias and variance for each AIRS and CrIMSS footprint is to tessellate a 240 km (approximately two degrees), hexagonal spatial grid over CONUS. We do this by creating a discrete global grid using the DGGRID software package (Sahr et al., 2003; Sahr, 2019). One of the centers, for example, is at 87.72550324 W, 40.7908839 N, near Watseka, Illinois; this center uniquely determines the tessellated grid. All elements of $\mathcal{A}^{kj}(d)$ are sorted in to these grid cells based on the instrument's footprint locations. Formally, let $i \in 1, \dots, L$ index grid cell centers, and let $1_i(\mathbf{u}) = 1$ if \mathbf{u} lies inside cell i , and zero otherwise. For grid cell i , mode j , and date d , set

$$\mathcal{A}_i^{kj}(d) = \left\{ \left\{ Z^I(\mathbf{s}, t_m^I(\mathbf{s})), Z^k(\mathbf{u}_{ms}^*, t^k(\mathbf{u}_{ms}^*)) : 1_i(\mathbf{u}_{ms}^*) = 1 \right\}_{m=1}^{M(d,j,\mathbf{s})} \right\}_{all \mathbf{s}},$$

732 where $M(d, j, \mathbf{s})$ is the number of time points acquired by the ISD station at \mathbf{s} on
 733 day d in mode j , L is the total number of hexagonal grid cells, and we write \mathbf{u}_{ms}^* to
 734 emphasize its dependence on m and \mathbf{s} via the matchup functions.

The bias assigned to all footprints from the k -th instrument observed on day d in mode j belonging to grid cell i is,

$$b_{dji}^k = \frac{1}{|\mathcal{A}_i^{kj}(d)|} \sum_{all \mathbf{s}} \sum_{m=1}^{M(d,j,\mathbf{s})} \left[Z^k(\mathbf{u}_{ms}^*, t^k(\mathbf{u}_{ms}^*)) - Z^I(\mathbf{s}, t_m^I(\mathbf{s})) \right] 1_i(\mathbf{u}_{ms}^*).$$

The corresponding variance assigned to all footprints observed on day d in mode j belonging to grid cell i is,

$$v_{dji}^k = \frac{1}{|\mathcal{A}_i^{kj}(d)|} \sum_{all \mathbf{s}} \sum_{m=1}^{M(d,j,\mathbf{s})} \left[Z^k(\mathbf{u}_{ms}^*, t^k(\mathbf{u}_{ms}^*)) - Z^I(\mathbf{s}, t_m^I(\mathbf{s})) - b_{dji}^k \right]^2 1_i(\mathbf{u}_{ms}^*),$$

Subtracting the biases from the satellite footprints yields bias-corrected data. Denote an footprint acquired by the k -th instrument on day d in mode j , centered at location \mathbf{u} , by $Z_{dji}^A(\mathbf{u})$, where we suppress the argument $t^A(\mathbf{u})$ since, for a given date and mode, location and time are confounded. The bias-corrected value is denoted by $Z_{dji}^{k*}(\mathbf{u})$ as follow:

$$Z_{dji}^{k*}(\mathbf{u}) = Z_{dji}^A(\mathbf{u}) - b_{dji^{i^*}}^A, \quad i^* = \operatorname{argmax}_i 1_i(\mathbf{u}),$$

735 with associated variance $v_{dji^{i^*}}^k$.

736 Appendix B SSDF methodology

737 Consider a discretized domain where $\{Y(\mathbf{s}) : \mathbf{s} \in D\}$ is a hidden, real-valued
 738 spatial observable. The domain of interest is $\cup\{A_i \subset \mathfrak{R}^d : i = 1, \dots, N_D\}$, which is
 739 made up of N_D fine-scale, non-overlapping, areal regions $\{A_i\}$ with locations $D \equiv$
 740 $\{\mathbf{p}_i \in A_i : i = 1, \dots, N_D\}$. Nguyen et al. (2012) call these fine-scale regions Basic
 741 Areal Units (BAUs), and they represent the smallest resolution at which we will make
 742 estimates with the model.

743 For a given day and mode (d and j using the notation of the previous subsection),
 744 denote the vector of NSAT data at all locations by \mathbf{Z}^k , where $k = 1$ for AIRS and
 745 $k = 2$ for CrIMSS:

$$\mathbf{Z}^k = (Z^k(B_{k1}), Z^k(B_{k2}), \dots, Z^k(B_{kN_k}))',$$

where \mathbf{Z}^k is N_k -dimensional, B_{kq} is the q -th footprint from the k -th dataset and is made up of BAUs with locations indexed by $D \cap B_{kq}$. We assume that data observed

at an arbitrary areal region B follow the “data model” in which the true observable is averaged over the areal region plus an independent error term. That is,

$$Z^k(B) = \frac{1}{|D \cap B|} \left\{ \sum_{\mathbf{s} \in D \cap B} Y(\mathbf{s}) \right\} + \epsilon^k(B); \quad B \subset \mathfrak{R}^d. \quad (\text{B1})$$

746 where $Y(\cdot)$ is a geophysical observable (here, NSAT) that is common to both datasets,
 747 and $\epsilon^k(\cdot)$ is an independent but non-identically distributed Gaussian random variable.
 748 That is, we assume that the q -th error in the k -th dataset is distributed as $\epsilon_q^k \sim$
 749 $N(b_q^k, v_q^k)$. In general, b_q^k is not zero, however, in our case b_q^k is assumed to be zero
 750 because we performed bias correction as described in the previous subsection, and
 751 v_q^k are calculated from the hexagonal-cell-specific mean and variance estimates (see
 752 Appendix A for details).

753 Our fused estimate for a region centered at location B_0 is a linear combination
 754 of \mathbf{Z}_1 and \mathbf{Z}_2 . That is,

$$\hat{Y}(B_0) = \mathbf{a}'_1 \mathbf{Z}_1 + \mathbf{a}'_2 \mathbf{Z}_2, \quad (\text{B2})$$

755 where \mathbf{a}_1 and \mathbf{a}_2 are N_1 and N_2 dimensional vectors, respectively. These vectors are
 756 unknown and are estimated in a way that minimizes the expected squared error relative
 757 to the true observable. That is, we choose \mathbf{a}_1 and \mathbf{a}_2 to minimize,

$$\begin{aligned} E((Y(B_0) - \hat{Y}(B_0))^2) &= \text{Var}(Y(B_0) - \mathbf{a}'_1 \mathbf{Z}_1 - \mathbf{a}'_2 \mathbf{Z}_2) \\ &= \text{Var}(Y(B_0)) - 2\mathbf{a}'_1 \text{Cov}(\mathbf{Z}_1, Y(B_0)) \\ &\quad - 2\mathbf{a}'_2 \text{Cov}(\mathbf{Z}_2, Y(B_0)) \\ &\quad - 2\mathbf{a}'_1 \text{Cov}(\mathbf{Z}_1, \mathbf{Z}_2) \mathbf{a}_2 \\ &\quad + \mathbf{a}'_1 \text{Var}(\mathbf{Z}_1) \mathbf{a}_1 + \mathbf{a}'_2 \text{Var}(\mathbf{Z}_2) \mathbf{a}_2 \end{aligned}$$

758 subject to the unbiasedness constraint that the elements of \mathbf{a}_1 and \mathbf{a}_2 add up to 1.
 759 That is,

$$\mathbf{1} = \mathbf{a}'_1 \mathbf{1}_{N_1} + \mathbf{a}'_2 \mathbf{1}_{N_2}, \quad (\text{B3})$$

760 where $\mathbf{1}_{N_k}$ is an N_k -dimensional vector of ones. The solution to the minimization
 761 problem in (B3) can be found via the method of Lagrange multipliers; but it requires
 762 knowledge of the spatial covariance structure $C(B_i, B_j)$, which can be expanded in
 763 terms of the BAU covariances:

$$C(B_i, B_j) = \frac{1}{|D \cap B_i| |D \cap B_j|} \sum_{\mathbf{u} \in D \cap B_i} \sum_{\mathbf{v} \in D \cap B_j} C(\mathbf{u}, \mathbf{v}). \quad (\text{B4})$$

Typically, the covariance structure in kriging-based approaches is estimated from the data, but the formulation in Equation B4 makes estimation intractable for non-linear covariance classes. We make use of the Spatial Mixed Effects model (SME; Cressie & Johannesson, 2008), which assumes that the true observable, here NSAT, can be written as the linear mixed model,

$$Y(\mathbf{s}) = \mathbf{t}(\mathbf{s})' \boldsymbol{\alpha} + \mathbf{S}(\mathbf{s})' \boldsymbol{\eta} + \xi(\mathbf{s}). \quad (\text{B5})$$

764 where $\mathbf{t}(\cdot) \equiv (t_1(\cdot), \dots, t_p(\cdot))'$ is a vector of p known covariates, such as geographical
 765 coordinates or other physical variables. The vector of linear coefficients, $\boldsymbol{\alpha}$, is unknown
 766 and will be estimated from the data. The middle term captures the spatial dependence
 767 as the product of an r -dimensional vector of known spatial basis functions, $\mathbf{S}(\mathbf{s})$, and an
 768 r -dimensional Gaussian random variable, $\boldsymbol{\eta}$. Here, we assume that with $\boldsymbol{\eta} \sim N(\mathbf{0}, \mathbf{K})$.
 769 Similar to the implementation in Nguyen et al. (2012), we implement these using
 770 multi-resolution bisquare basis functions centered at different resolutions of the Inverse

771 Snyder Equal-Area Projection Aperture 3 Hexagon (ISEA3H) type within the Discrete
 772 Global Grid (DGGRID) software (specifically, resolutions 2, 3, and 5 of ISEA3H, for
 773 details see Sahr, 2019). The last term, $\xi(\cdot)$, describes the BAU-scale variability of the
 774 process. We assume that $\xi(\cdot)$ is an independent Gaussian process with mean zero and
 775 variance σ_ξ^2 .

776 The SME model in Equation B5 has useful change-of-support properties, which
 777 makes computation of the spatial covariance function straightforward. In particular,
 778 Nguyen et al. (2012) shows that

$$\text{cov}(Z(B_i), Z(B_j)) = \mathbf{S}(B_i)' \mathbf{K} \mathbf{S}(B_j) + \sigma_\xi^2 \frac{|D \cap B_i \cap B_j|}{|D \cap B_i| |D \cap B_j|} + v_i^k I(i = j), \quad (\text{B6})$$

where

$$\mathbf{S}(B_i) \equiv \frac{1}{|D \cap B_i|} \sum_{\mathbf{u} \in D \cap B_i} \mathbf{S}(\mathbf{u}).$$

779 Notice that Equation B6 allows us to express the covariance between spatial averages
 780 *explicitly* in terms of the spatial dependence parameter \mathbf{K} . This allows for straightfor-
 781 ward estimation of it from footprint data.

782 Another advantage of the SME model is its scalability. For a general covariance
 783 structure, solving for \mathbf{a}_1 and \mathbf{a}_2 requires inverting a $(N_1 + N_2) \times (N_1 + N_2)$ covariance
 784 matrix, which has computational complexity $O((N_1 + N_2)^3)$. For large datasets such
 785 as AIRS and CrIMSS where the data size is on the order of tens of thousands, this
 786 matrix inversion is computationally infeasible. However, the model in Equation B5
 787 implies the following full covariance matrix:

$$\begin{aligned} \Sigma &\equiv \text{var}((\mathbf{Z}^{1'}, \mathbf{Z}^{2'})') \\ &= \mathbf{S}' \mathbf{K} \mathbf{S} + \mathbf{U}, \end{aligned}$$

788 where \mathbf{S} is a matrix constructed by appending the spatial function $\mathbf{S}(\cdot)$ over all the
 789 footprints in both datasets, \mathbf{U} is the *sparse* covariance matrix for the fine-scale pro-
 790 cesses $\xi(\cdot)$, and the measurement-error processes $\epsilon^k(\cdot)$ at the given data locations (for
 791 more details, see Equation 4 of Nguyen et al., 2012). Using the Sherman-Morrison-
 792 Woodbury formula (e.g., Henderson & Searle, 1981), the matrix inverse is given by,

$$\Sigma^{-1} = \mathbf{U}^{-1} - \mathbf{U}^{-1} \mathbf{S}' (\mathbf{K}^{-1} + \mathbf{S} \mathbf{U}^{-1} \mathbf{S}')^{-1} \mathbf{S} \mathbf{U}^{-1},$$

793 Note that the inversion above, and hence the calculation of the coefficients \mathbf{a}_1 and
 794 \mathbf{a}_2 for the fused estimate, is very fast because it only requires inversion of the *sparse*
 795 $(N_1 + N_2) \times (N_1 + N_2)$ matrix \mathbf{U} , which is typically very sparse, and inversion of \mathbf{K}
 796 and $(\mathbf{K}^{-1} + \mathbf{S}' \mathbf{U}^{-1} \mathbf{S})$, both of which are $r \times r$ matrices ($r \ll N_1 + N_2$).

797 References

- 798 AIRS Project. (2019). *Aqua/AIRS L2 Standard Physical Retrieval (AIRS-*
 799 *only) V7.0*. Goddard Earth Sciences Data and Information Services Cen-
 800 ter (GES DISC). Greenbelt, MD, USA. (Accessed: 2019-2021) doi:
 801 10.5067/VP1M6OG1X7M1
- 802 AIRS Project. (2020). *About the data*. Retrieved 2021-12-26, from [https://airs](https://airs.jpl.nasa.gov/data/about-the-data/granules/)
 803 [.jpl.nasa.gov/data/about-the-data/granules/](https://airs.jpl.nasa.gov/data/about-the-data/granules/)
- 804 AIRS team. (n.d.). *About the products*. Retrieved from [https://airs.jpl.nasa](https://airs.jpl.nasa.gov/data/products/retrieval-systems/)
 805 [.gov/data/products/retrieval-systems/](https://airs.jpl.nasa.gov/data/products/retrieval-systems/) (accessed: June 3, 2022)
- 806 Barnet, C. (2019). *Sounder SIPS: Suomi NPP CrIMSS Level 2 CLIMCAPS normal*
 807 *spectral resolution: Cloud cleared radiances v2*. Goddard Earth Sciences Data
 808 and Information Services Center (GES DISC). Greenbelt, MD, USA. (Ac-
 809 cessed: 2019-2021) doi: 10.5067/CNG0ST72533Z

- 810 Blackwell, W. (2005). A neural-network technique for the retrieval of atmospheric
 811 temperature and moisture profiles from high spectral resolution sounding data.
 812 *Geoscience and Remote Sensing, IEEE Transactions on*, 43(11), 2535-2546.
 813 doi: 10.1109/TGRS.2005.855071
- 814 Braverman, A., Hobbs, J., Teixeira, J., & Gunson, M. (2021). Post hoc uncertainty
 815 quantification for remote sensing observing systems. *SIAM/ASA Journal on*
 816 *Uncertainty Quantification*, 9(3), 1064-1093.
- 817 Chahine, M. T., Pagano, T. S., Aumann, H. H., Atlas, R., Barnet, C., Blaisdell, J.,
 818 ... Zhou, L. (2006). AIRS: Improving weather forecasting and providing new
 819 data on greenhouse gases. *Bulletin of the American Meteorological Society*,
 820 87(7), 911-926.
- 821 Cressie, N. (1993). *Statistics for spatial data*. John Wiley & Sons.
- 822 Cressie, N., & Johannesson, G. (2008). Fixed rank kriging for very large spatial data
 823 sets. *Journal of the Royal Statistical Society: Series B (Statistical Methodol-*
 824 *ogy)*, 70(1), 209-226.
- 825 Ferguson, C. R., & Wood, E. F. (2010). An evaluation of satellite remote sensing
 826 data products for land surface hydrology: Atmospheric infrared sounder. *Jour-*
 827 *nal of Hydrometeorology*, 11(6), 1234-1262.
- 828 Ghamisi, P., Rasti, B., Yokoya, N., Wang, Q., Hofle, B., Bruzzone, L., ... others
 829 (2019). Multisource and multitemporal data fusion in remote sensing: A
 830 comprehensive review of the state of the art. *IEEE Geoscience and Remote*
 831 *Sensing Magazine*, 7(1), 6-39.
- 832 Good, E. (2015). Daily minimum and maximum surface air temperatures from
 833 geostationary satellite data. *Journal of Geophysical Research: Atmospheres*,
 834 120(6), 2306-2324.
- 835 Gotway, C. A., & Young, L. J. (2002). Combining incompatible spatial data.
 836 *Journal of the American Statistical Association*, 97(458), 632-648. doi:
 837 10.1198/016214502760047140
- 838 Hammerling, D. M., Michalak, A. M., & Kawa, S. R. (2012). Mapping of CO₂ at
 839 high spatiotemporal resolution using satellite observations: Global distribu-
 840 tions from OCO-2. *Journal of Geophysical Research: Atmospheres*, 117(D6).
- 841 Harrison, G., & Burt, S. D. (2021). Quantifying uncertainties in climate data: mea-
 842 surement limitations of naturally ventilated thermometer screens. *Environmen-*
 843 *tal Research Communications*.
- 844 Henderson, H., & Searle, S. (1981). On deriving the inverse of a sum of matrices.
 845 *SIAM Review*, 23, 53-60.
- 846 Hennermann, K., & Berrisford, P. (2019). *ERA5 data documentation*, ECMWF.
- 847 Hobbs, J., Braverman, A., Cressie, N., Granat, R., & Gunson, M. (2017).
 848 Simulation-based uncertainty quantification for estimating atmospheric CO₂
 849 from satellite data. *SIAM/ASA Journal on Uncertainty Quantification*, 5(1),
 850 956-985.
- 851 Kendall, M. G. (1948). Rank correlation methods.
- 852 Mann, H. B. (1945). Nonparametric tests against trend. *Econometrica: Journal of*
 853 *the econometric society*, 245-259.
- 854 McNally, A. P., Watts, P. D., A. Smith, J., Engelen, R., Kelly, G. A., Thépaut,
 855 J. N., & Matricardi, M. (2006). The assimilation of AIRS radiance data at
 856 ECMWF. *Quarterly Journal of the Royal Meteorological Society*, 132(616),
 857 935-957. Retrieved from <http://dx.doi.org/10.1256/qj.04.171> doi:
 858 10.1256/qj.04.171
- 859 Nguyen, H., Cressie, N., & Braverman, A. (2012). Spatial statistical data fusion
 860 for remote sensing applications. *Journal of the American Statistical Asso-*
 861 *ciation*, 107(499), 1004-1018. Retrieved from [https://doi.org/10.1080/](https://doi.org/10.1080/01621459.2012.694717)
 862 [01621459.2012.694717](https://doi.org/10.1080/01621459.2012.694717) doi: 10.1080/01621459.2012.694717
- 863 Nguyen, H., Katzfuss, M., Cressie, N., & Braverman, A. (2014). Spatio-temporal
 864 data fusion for very large remote sensing datasets. *Technometrics*, 56(2), 174-

- 185.
- 865 Olsen, E. T., Fishbein, E., Manning, E., & Maddy, E. (2017). AIRS/AMSU/HSB
866 Version 6 L2 product levels, layers and trapezoids. *Jet Propulsion Laboratory,*
867 *Pasadena, CA, USA.*
- 869 Rayner, N. A., Auchmann, R., Bessembinder, J., Brönnimann, S., Brugnara, Y.,
870 Capponi, F., . . . others (2020). The eustace project: delivering global, daily
871 information on surface air temperature. *Bulletin of the American Meteorologi-*
872 *cal Society, 101*(11), E1924–E1947.
- 873 Rohde, R. A., & Hausfather, Z. (2020). The berkeley earth land/ocean temperature
874 record. *Earth System Science Data, 12*(4), 3469–3479.
- 875 Sahr, K. (2019). *Dggrid version 7.0: User documentation for discrete global grid*
876 *software.*
- 877 Sahr, K., White, D., & Kimerling, A. J. (2003). Geodesic discrete global grid sys-
878 tems. *Cartography and Geographic Information Science, 30*(2), 121–134.
- 879 Sen, P. K. (1968). Estimates of the regression coefficient based on kendall’s tau.
880 *Journal of the American statistical association, 63*(324), 1379–1389.
- 881 Smith, A., Lott, N., & Vose, R. (2011). The integrated surface database: Recent de-
882 velopments and partnerships. *Bulletin of the American Meteorological Society,*
883 *92*(6), 704–708.
- 884 Smith, N., & Barnett, C. D. (2019). Uncertainty characterization and propagation
885 in the Community Long-Term Infrared Microwave Combined Atmospheric
886 Product System (CLIMCAPS). *Remote Sensing, 11*(10), 1227.
- 887 Smith, N., & Barnett, C. D. (2020). CLIMCAPS observing capability for temper-
888 ature, moisture, and trace gases from AIRS/AMSU and CrIS/ATMS. *Atmo-*
889 *spheric Measurement Techniques, 13*(8), 4437–4459.
- 890 Sun, J., McColl, K. A., Wang, Y., Rigden, A. J., Lu, H., Yang, K., . . . Santanello Jr,
891 J. A. (2021). Global evaluation of terrestrial near-surface air temperature
892 and specific humidity retrievals from the atmospheric infrared sounder (airs).
893 *Remote Sensing of Environment, 252,* 112146.
- 894 Susskind, J., Blaisdell, J. M., & Iredell, L. (2014). Improved methodology for
895 surface and atmospheric soundings, error estimates, and quality control pro-
896 cedures: the atmospheric infrared sounder science team version-6 retrieval
897 algorithm. *Journal of Applied Remote Sensing, 8*(1), 084994. Retrieved from
898 <http://dx.doi.org/10.1117/1.JRS.8.084994> doi: 10.1117/1.JRS.8.084994
- 899 Thrastarson, H. T., Manning, E., Kahn, B., Fetzer, E., Yue, Q., Wong, S., . . . others
900 (2020). AIRS/AMSU/HSB Version 7 Level 2 product user guide. *Jet Propul-*
901 *sion Laboratory, California Institute of Technology: Pasadena, CA, USA,*
902 83–92.
- 903 Wilks, D. S. (2006). *Statistical methods in the atmospheric sciences* (Second ed.).
904 Burlington, MA: Academic Press.
- 905 Yue, Q., Lambrigtsen, B., et al. (2017). AIRS V6 test report supplement: Perform-
906 ance of AIRS+AMSU vs. AIRS-only retrievals. *Jet Propulsion Laboratory,*
907 *California Institute of Technology: Pasadena, CA, USA.* Retrieved from
908 [https://docserver.gesdisc.eosdis.nasa.gov/repository/Mission/](https://docserver.gesdisc.eosdis.nasa.gov/repository/Mission/AIRS/3.3.ScienceDataProductDocumentation/3.3.5.ProductQuality/V6_Test_Report_Supplement_Performance_of_AIRS+AMSU_vs_AIRS-Only_Retrievals.pdf)
909 [AIRS/3.3.ScienceDataProductDocumentation/3.3.5.ProductQuality/](https://docserver.gesdisc.eosdis.nasa.gov/repository/Mission/AIRS/3.3.ScienceDataProductDocumentation/3.3.5.ProductQuality/V6_Test_Report_Supplement_Performance_of_AIRS+AMSU_vs_AIRS-Only_Retrievals.pdf)
910 [V6_Test_Report_Supplement_Performance_of_AIRS+AMSU_vs_AIRS-Only](https://docserver.gesdisc.eosdis.nasa.gov/repository/Mission/AIRS/3.3.ScienceDataProductDocumentation/3.3.5.ProductQuality/V6_Test_Report_Supplement_Performance_of_AIRS+AMSU_vs_AIRS-Only_Retrievals.pdf)
911 [_Retrievals.pdf](https://docserver.gesdisc.eosdis.nasa.gov/repository/Mission/AIRS/3.3.ScienceDataProductDocumentation/3.3.5.ProductQuality/V6_Test_Report_Supplement_Performance_of_AIRS+AMSU_vs_AIRS-Only_Retrievals.pdf)
- 912 Yue, Q., Lambrigtsen, B., et al. (2020). AIRS V7 L2 performance test and vali-
913 dation report. *Jet Propulsion Laboratory, California Institute of Technology:*
914 *Pasadena, CA, USA.* Retrieved from [https://docserver.gesdisc.eosdis](https://docserver.gesdisc.eosdis.nasa.gov/public/project/AIRS/V7_L2_Performance_Test_and_Validation_report.pdf)
915 [.nasa.gov/public/project/AIRS/V7_L2_Performance_Test_and_Validation](https://docserver.gesdisc.eosdis.nasa.gov/public/project/AIRS/V7_L2_Performance_Test_and_Validation_report.pdf)
916 [_report.pdf](https://docserver.gesdisc.eosdis.nasa.gov/public/project/AIRS/V7_L2_Performance_Test_and_Validation_report.pdf)
- 917 Yue, Q., Lambrigtsen, B., et al. (2021). Version 2 CLIMCAPS-Aqua re-
918 trieval product performance test report. *Jet Propulsion Laboratory, Cal-*
919 *ifornia Institute of Technology: Pasadena, CA, USA.* Retrieved from

920

[https://docserver.gesdisc.eosdis.nasa.gov/public/project/Sounder/
CLIMCAPS.V2.Test.Report.Aqua.pdf](https://docserver.gesdisc.eosdis.nasa.gov/public/project/Sounder/CLIMCAPS.V2.Test.Report.Aqua.pdf)

921